

DISSERTATION

BAYESIAN APPROACH TO THE ANISOTROPIC EIT PROBLEM AND EFFECT OF
STRUCTURAL CHANGES ON RECONSTRUCTION ALGORITHM USING 2-D D-BAR
ALGORITHM

Submitted by

Rashmi Murthy

Department of Mathematics

In partial fulfillment of the requirements

For the Degree of Doctor of Philosophy

Colorado State University

Fort Collins, Colorado

Summer 2018

Doctoral Committee:

Advisor: Jennifer L. Mueller

Margaret Cheney

Oliver Pinaud

Kristen Buchanan

Copyright by Rashmi Murthy 2018

All Rights Reserved

ABSTRACT

BAYESIAN APPROACH TO THE ANISOTROPIC EIT PROBLEM AND EFFECT OF STRUCTURAL CHANGES ON RECONSTRUCTION ALGORITHM USING 2-D D-BAR ALGORITHM

Electrical Impedance Tomography (EIT) is a relatively new imaging technique that is non-invasive, low-cost, and non-ionizing with excellent temporal resolution. In EIT, the unknown electrical conductivity in the interior of the medium is determined from the boundary electrical measurements. In this work, we attempt to find a direct reconstruction algorithm to the anisotropic EIT problem based on the well-known Calderón's method. The non-uniqueness of the inverse problem is dealt with assuming that the directions of anisotropy are known. We utilize the quasi-conformal map in the plane to accomplish Calderón's approach. Additionally, we derive a probability distribution for the anisotropic conductivity values using a Bayesian formulation, where the direction of anisotropy is encoded as the prior information. We show that this results in the generalized Tikhonov regularization, where the prior information about the direction of anisotropy is incorporated in the regularization operator. The computations of the anisotropic EIT problem using the Bayesian formulation is conducted on simulated data and the resulting reconstructions for the data are shown. Finally, the work of this thesis is concluded by implementing dynamic changes in boundary of a human data during respiration process successfully in the D-bar algorithm.

ACKNOWLEDGEMENTS

I would like to thank my advisor Jennifer Mueller for her extensive guidance and support on and off academic matters over the years that I have been away from home. Additional thanks go to members of Electrical Impedance Tomography group student members. I would also like to thank my family for their support and encouragement in my academic journey.

TABLE OF CONTENTS

| | |
|--|-----|
| ABSTRACT | ii |
| ACKNOWLEDGEMENTS | iii |
| LIST OF TABLES | vi |
| LIST OF FIGURES | vii |
| | |
| Chapter 1 Introduction | 1 |
| 1.1 Electrical Impedance Tomography | 1 |
| 1.1.1 Advantages of EIT | 2 |
| 1.1.2 Applications of EIT | 2 |
| 1.2 Mathematical Formulation of EIT | 4 |
| 1.2.1 Continuum Boundary Conditions | 4 |
| 1.2.2 Nonlinearity of EIT | 6 |
| 1.2.3 Ill-posedness of EIT | 6 |
| 1.2.4 Data Aquisition in EIT | 7 |
| 1.2.5 Electrode Models | 7 |
| 1.2.6 Current Patterns | 9 |
| 1.3 Numerical solution to the forward EIT problem | 10 |
| 1.4 Literature Review | 15 |
| 1.4.1 Calderón’s Problem | 15 |
| 1.4.2 Further developments on inverse conductivity problem | 16 |
| 1.4.3 Reconstruction algorithms and computation | 17 |
| | |
| Chapter 2 Anisotropic inverse conductivity problem | 22 |
| 2.1 Introduction | 22 |
| 2.2 Mathematical model of the anisotropic EIT problem | 23 |
| 2.3 Difficulties of anisotropic inverse conductivity problem | 24 |
| 2.3.1 History of the problem | 24 |
| 2.3.2 Further developments in anisotropic inverse conductivity problem | 25 |
| 2.4 Injectivity for the linearized anisotropic inverse conductivity problem based on Calderón’s method | 26 |
| 2.5 Bayesian formulation of the anisotropic EIT problem | 34 |
| 2.6 Forward anisotropic EIT problem | 35 |
| 2.6.1 Variational formulation of the anisotropic EIT | 36 |
| 2.6.2 Finite Element Formulation of anisotropic EIT | 36 |
| 2.7 Inverse problem | 41 |
| 2.7.1 Construction of Priors | 42 |
| 2.7.2 Numerical implementation | 44 |
| 2.7.3 Computation of the Jacobian | 45 |
| 2.7.4 Implementation of the reconstruction algorithm | 45 |
| 2.8 Conclusions and Future work | 46 |

| | | |
|--------------|--|----|
| Chapter 3 | Impact of structural changes in the reconstruction using 2-D D-bar algorithm | 48 |
| 3.1 | Introduction | 48 |
| 3.2 | Literature Review | 48 |
| 3.2.1 | Effect of domain shape on reconstruction | 48 |
| 3.2.2 | Effect of dynamic changes in the boundary on reconstruction | 49 |
| 3.3 | Implementation of dynamic changes in boundary | 51 |
| 3.4 | Results | 53 |
| 3.5 | Discussions | 55 |
| 3.6 | Conclusions | 56 |
| Bibliography | | 59 |

LIST OF TABLES

| | | |
|-----|---|----|
| 1.1 | Conductivity and permittivity values for various tissues and organs. (source: Linear and Nonlinear Inverse Problems with Applications [97]) | 3 |
| 2.1 | Conductivities in perpendicular and parallel directions on the pial surface of neocortex. (Source: [4]) | 23 |

LIST OF FIGURES

| | | |
|-----|--|----|
| 1.1 | Human Thoracic 2-D EIT data collection, with electrodes arranged in a plane around the patient's thorax. | 2 |
| 2.1 | The placement of electrodes on the exterior of a circular domain with a circular inclusion shown in red. Here the first electrode is placed on the horizontal axis at 0 degrees and the electrodes are counted counter clockwise. The conductivity is given by σ_{int}^{ver} inside the circular inclusion and σ_1 in the annulus outside the circular inclusion. | 40 |
| 2.2 | Left: The potential on the 32 electrodes due to 31 linearly independent current patterns applied to the electrodes when the conductivity in the circular inclusion is assumed to be σ_{int}^{ver} . Right: The potential on the 32 electrodes due to 31 linearly independent current patterns applied to the electrodes when the conductivity in the circular inclusion is assumed to be σ_{int}^{hor} . Each color represents a voltage arising from a different current pattern. | 41 |
| 2.3 | Left: Reconstruction of the diagonal conductivity along the x-axis d_1 . Right: Reconstruction of the diagonal conductivity along the y-axis d_2 . It is clear that d_1 is less than that of d_2 values. | 46 |
| 3.1 | Change in the overall cross-sectional area during inhalation and exhalation. (Source: [120]) | 49 |
| 3.2 | The EIT data collected during a spirometry test. | 50 |
| 3.3 | PCA output during a spirometry test used for identifying the key time points for the implementation of the dynamically changing boundary. TLC on the plot corresponds to the maximum inhalation and EFE corresponds to maximum exhalation. | 52 |
| 3.4 | Plots of reconstructions of the conductivity that corresponding to first frame, the first exhalation, first inhalation, consequent exhalation, maximum inhalation and maximum exhalation and the consecutive breaths | 54 |
| 3.5 | Plots of reconstructions of the conductivity that corresponding to first frame, the first exhalation, first inhalation, consequent exhalation, maximum inhalation and maximum exhalation and the consecutive breaths | 55 |
| 3.6 | The reconstructions of the EIT data for the same subject with and without accounting for dynamically changing boundary. | 56 |
| 3.7 | The reconstructions of the EIT data for the same subject with and without accounting for dynamically changing boundary. | 57 |
| 3.8 | Difference in the conductivity computed with and without the dynamically changing boundary values for frames 36,93,148,229 | 58 |

Chapter 1

Introduction

1.1 Electrical Impedance Tomography

Electrical impedance tomography (EIT) is a relatively new medical imaging technique in which the internal electrical properties such as conductivity σ , permittivity ϵ , or resistivity $\rho = 1/\sigma$ of an object are reconstructed using current density and voltage measurements on the surface of the object. In data acquisition, current of the order of mA are applied to the electrodes on the boundary, and the resulting potentials on the electrodes of the order of hundreds of mV are measured. Inhomogeneities in the internal electrical properties results in the perturbations in the surface voltage measurements from the homogeneous case. This can be used to reconstruct an image of the object's internal structures.

This thesis addresses two problems, first one being the problem of anisotropic EIT. Although, the problem of EIT is well studied when the conductivity is isotropic, the anisotropic EIT problem has not been given its due. One reason for this is the fact that the solution to the anisotropic EIT is not unique. To overcome the problem of non unique solution to the anisotropic EIT, we make assumptions on the nature of anisotropy. That is we assume that the direction of preference of the conductivity is known. We then formulate the mathematical problem of anisotropic EIT and in the spirit of Calderón show the injectivity of the linearized anisotropic inverse conductivity problem. In addition to this we formulate the problem of anisotropic EIT in Bayesian setting. In this approach, we construct the priors for the anisotropic conductivity using the fact that the direction of the conductivity tensor is known, and show that the Bayesian formulation leads to the generalized Tikhonov regularization. We solve this optimization problem to get maximum a posterior estimates for the conductivity values. Second, we incorporate the dynamic structural changes to the 2-D D-bar algorithm and successfully implement them on the human data.

1.1.1 Advantages of EIT

EIT is an attractive option for many imaging tasks since the equipment is cost effective, electrical currents can penetrate through many materials without damaging them and fast electronics are available for real time applications.

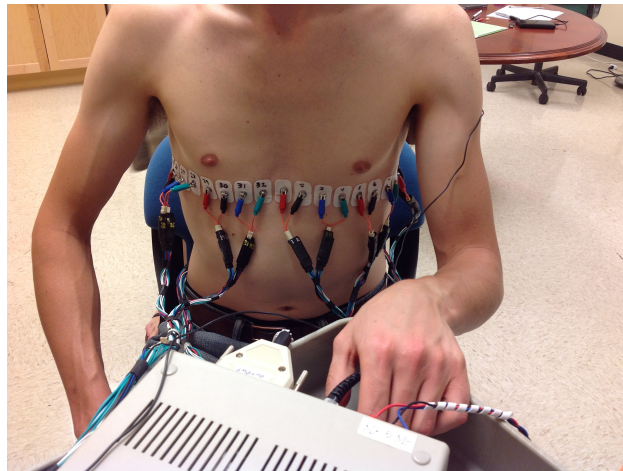


Figure 1.1: Human Thoracic 2-D EIT data collection, with electrodes arranged in a plane around the patient's thorax.

1.1.2 Applications of EIT

There are a variety of applications of EIT, including medical, engineering and industrial, and new applications continue to emerge. The original motivation for EIT was the prospection of the underground natural resources [35]. These days EIT is used in a number of geophysical applications such as subsurface flow monitoring and remediation [44, 46, 87, 107] and underground contamination detection [47, 85, 87, 108]. In industrial applications, process tomography may be used to understand the complex internal flows and multiphase mixtures occurring inside process equipment. In this regard, EIT has been applied to pharmaceutical testing [24, 109, 110], mixture and flow monitoring [50, 77, 89, 92], contaminant detection [93], nondestructive evaluation of concrete and other structures [45, 74, 79, 81], and various other process applications [84, 118].

In this dissertation, however, EIT is in the context of medical imaging applications. Medical EIT relies on the fact that the conductivity and permittivity of various tissues and organs in the body are measurable and have significant differences as shown in the Table 1.1

Table 1.1: Conductivity and permittivity values for various tissues and organs. (source: Linear and Nonlinear Inverse Problems with Applications [97])

| Tissue | Conductivity(mS/cm) | Permittivity(μ F/m) |
|------------------------------|---------------------|--------------------------|
| Blood | 6.70 | 0.05 |
| Liver | 2.80 | 0.49 |
| Bone | 0.06 | 0.0027 |
| Cardiac Muscle(Longitudinal) | 6.3 | 0.88 |
| Cardiac Muscle(Transversal) | 2.3 | 0.36 |
| Lung(expiration) | 1.0 | 0.44 |
| Lung(inspiration) | 0.4 | 0.22 |
| Fat | 0.36 | 0.18 |
| Skin | 0.0012 | 0.0144 |

In the field of medical imaging there are various imaging techniques available, each with its own advantages and disadvantages. Techniques such as magnetic resonance imaging (MRI) and X-ray computed tomography (CT) have the advantage of very good spatial resolution but require large, expensive and non portable machines. CT scanning has the additional disadvantage of the use of ionizing radiation. Ultrasound is safer and more portable, however, it is quite low contrast and difficult to use on obese patients due to limitations in the depth of ultrasound penetration. EIT has the potential of providing inexpensive, portable, high-contrast, real-time imaging with excellent temporal resolution. The procedure is painless and does not expose patients to ionizing radiation.

There is a long, diverse and ever-growing list of promising medical applications of EIT. A variety of research groups have evaluated EIT for use in breast cancer detection, based on evidence that malignant tumors have higher conductivity values than surrounding normal tissues [42, 43]. Some of the biomedical applications of EIT are: it can be used to monitor cardiac activity and

diagnosis of pulmonary embolism [41, 82, 94, 105, 111, 117], ventilation and lung perfusion monitoring [62, 63, 65], gastric emptying and gastric volume [80], diagnosis of pulmonary edema [31] prostate imaging [27, 28], and assessment of stroke and other neural imaging [2, 12, 54, 71, 80].

The EIT lab in the Department of Mathematics at Colorado State University focuses on the 2-D thoracic imaging. This is accomplished by collecting data on approximately equally-spaced electrodes that are placed in a single plane around the circumference of a human chest. To these electrodes a low frequency, low amplitude AC current is applied and the resulting surface voltages are measured, which provides the necessary data to reconstruct the electrical conductivity distribution within the plane of the electrodes.

1.2 Mathematical Formulation of EIT

The propagation of electromagnetic fields in a body is governed by Maxwell's equations. Due to the very small magnetic permeability of the human body, and the low frequency time-harmonic currents that are applied in EIT, Maxwell's equations can be simplified to the generalized Laplace equation. That is:

$$\nabla(\sigma(x, y)\nabla u(x, y)) = 0 \quad (x, y) \in \Omega, \quad (1.1)$$

where $\Omega \subset \mathbb{R}^2$ is a bounded, simply connected domain with Lipschitz boundary, $\sigma : \Omega \rightarrow \mathbb{R}$ is the electrical conductivity distribution within Ω , and $u : \Omega \rightarrow \mathbb{R}$ is the electrical potential within Ω . The complete derivation is presented in [97]. Furthermore, conductivity σ is bounded away from zero, such that $0 < \sigma < c$ for all $(x, y) \in \Omega$. This condition ensures that (1.1) is elliptic.

1.2.1 Continuum Boundary Conditions

If the voltage distribution $f = f(x, y)$ on the boundary $\partial\Omega$ is known, then we have the Dirichelet boundary condition:

$$u|_{\partial\Omega} = f \quad (1.2)$$

The resulting current density distribution J on the boundary is measured:

$$J(x, y) \cdot \nu = \sigma(x, y) \frac{\partial u(x, y)}{\partial \nu} = j \quad (1.3)$$

where ν is the outward unit normal vector.

The Dirichlet to Neumann map (DN map), also known as voltage to current density map, denoted by Λ_σ , takes the voltage distribution to the current density distribution:

$$\Lambda_\sigma : u|_{\partial\Omega} \rightarrow \sigma \frac{\partial u}{\partial \nu} \Big|_{\partial\Omega} \quad (1.4)$$

If $\sigma \in L^\infty(\Omega)$, then it can be shown that the linear operator Λ_σ is bounded between the Sobolev spaces:

$$\Lambda_\sigma : H^{1/2}(\partial\Omega) \rightarrow H^{-1/2}(\partial\Omega).$$

The DN map contains all possible EIT boundary measurements with infinite precision.

On the other hand, if current is applied on the boundary $\partial\Omega$ and the resulting voltage distribution on the boundary is measured, then this corresponds to knowledge of the Neumann to Dirichlet map (ND map) \mathcal{R} defined by

$$\mathcal{R}_\sigma : \sigma \frac{\partial u}{\partial \nu} \Big|_{\partial\Omega} \rightarrow u|_{\partial\Omega} \quad (1.5)$$

and it is bounded between the Sobolev spaces:

$$\mathcal{R}_\sigma : \tilde{H}^{-1/2}(\partial\Omega) \rightarrow \tilde{H}^{1/2}(\partial\Omega)$$

where \tilde{H}^s spaces consists of H^s functions with mean value zero.

The forward conductivity problem is to determine $u \in H^1(\Omega)$ by solving (1.1) subject to Dirichlet condition (1.2). This requires the knowledge of σ inside the domain, Ω . The forward problem can be solved numerically using, for example, Finite Element Methods.

The imaging problem of EIT is the inverse conductivity problem, where we are interested in recovering the unknown conductivity σ uniquely, satisfying (1.1), given the knowledge of DN map (1.4).

1.2.2 Nonlinearity of EIT

The problem of EIT is nonlinear, since the forward mapping $\sigma \mapsto \Lambda_\sigma$ is nonlinear. This can be established by using the weak form of DN map.

$$\langle \Lambda_\sigma u, j \rangle = \int_{\Omega} \sigma \nabla u \cdot \nabla v dx dy \quad (1.6)$$

Since u itself is a function of σ , it is clear from (1.6), that the DN map (1.4) is a nonlinear function of σ . The current densities on the electrodes are non linear functions of the conductivity σ . This is in contrast with the X-ray tomography, where the measured data depends linearly on the density of the medium.

1.2.3 Ill-posedness of EIT

EIT is severely ill-posed in the sense that the solution does not depend continuously on data. That is, the forward map $\sigma \mapsto \Lambda_\sigma$ does not have a continuous inverse. This means that large changes in internal conductivity distribution may result in negligible changes in the boundary measurements (DN map). Thus, for any given finite measurement precision, there will exist distinct conductivity distributions that lead to indistinguishable boundary current and voltage measurements. This was established by Alessandrini in [5].

This leads to the EIT problem being very mathematically challenging. Apart from the mathematical challenges of EIT, there are other various practical problems related to electrical properties of the physical domain and imperfections of electronics and hardware [3]. We are interested in the conductivity changes deep inside the interior of the domain, but only a relatively small amount of the applied current penetrates deeply. In medical applications this effect is exacerbated by resistive tissues such as bone, lungs, or fat. EIT is also highly sensitive to any imperfections in hardware or difficulties with electrode contact.

1.2.4 Data Acquisition in EIT

The continuum models given by equations (1.4) and (1.5) is an idealization and does not take into account that in practice current is applied through a finite number of electrodes on the surface of the body and not as a continuous current density along the boundary. For L electrodes, there are N linearly independent current patterns where $N \leq L - 1$. In the EIT lab at Colorado State University, the ACE1 EIT machine is used to collect experimental data, and has been designed to apply bipolar skip patterns [97]. Application of a skip s pattern on L electrodes results in $N = L - \gcd(L, s + 1)$ linearly independent measurements.

1.2.5 Electrode Models

The model given by (1.4) and (1.5) does not take into account that in practice current is applied only through a finite number of electrodes on the surface of the domain. Various models have been proposed to simulate the experimental situation and can be found in [97]. Below are the description of some of the electrode models commonly used in EIT literature.

- i. The Gap Model: The Gap model sets the current density J as 0 off the electrode and current density on the l th electrode e_l is taken to be the current on electrode e_l divided by area of the l th electrode.

$$J(z) = \begin{cases} \frac{I_l}{A_l}, & \text{if } z \text{ lies on electrode } e_l, l = 1, \dots, L, \\ 0, & \text{off } \bigcup_{l=1}^L e_l. \end{cases} \quad (1.7)$$

The conservation of charge (1.3) is replaced by conservation of currents,

$$\sum_{l=1}^L I_l = 0 \quad (1.8)$$

Voltages that are measured are assumed to have potential at the center of each electrode

$$u(\text{center of } e_l) = V_l \quad (1.9)$$

with the reference potential being set so that

$$\sum_{l=1}^L V_l = 0. \quad (1.10)$$

- ii. The Shunt Model: The gap model does not take into account the shunting effect of electrodes when they are in contact with the surface of the medium being imaged. To overcome this problem, the voltage is assumed to be a constant over the electrode by assuming the electrode as a perfect conductor. The mathematical model is described as follows:

$$u(z) = V_l \quad \text{for } z \text{ on } e_l, \quad l = 1, 2, \dots, L, \quad (1.11)$$

and

$$u(z) = 0 \quad \text{off} \quad \bigcup_{l=1}^L e_l \quad (1.12)$$

along with

$$\int_{e_l} \sigma \frac{\partial u}{\partial \nu} ds = I_l, \quad l = 1, 2, \dots, L, \quad (1.13)$$

and

$$\sigma \frac{\partial u}{\partial \nu} = 0 \quad \text{off} \quad \bigcup_{l=1}^L e_l \quad (1.14)$$

- iii. The Complete Electrode Model: With human subjects, an electrochemical effect between the electrode and the skin causes a thin, highly resistive layer to form at the electrode - skin interface with impedance z_l , known as contact impedance. This gives rise to a Robin boundary condition,

$$u + z_l \sigma \frac{\partial u}{\partial \nu} = V_l \quad \text{on} \quad e_l, \quad l = 1, 2, \dots, L. \quad (1.15)$$

Along with the Robin boundary condition, the condition on the applied current in complete electrode model is given by,

$$\int_{e_l} \sigma \frac{\partial u}{\partial \nu} ds = I_l, \quad l = 1, 2, \dots, L,$$

$$\sigma \frac{\partial u}{\partial \nu} = 0, \quad \text{off} \quad \bigcup_{l=1}^L e_l$$

The unique solution specifies the choice of ground by

$$\sum_{l=1}^L U_l = 0,$$

and Kirchhoff's law,

$$\sum_{l=1}^L I_l = 0.$$

A detailed discussion of the complete electrode model for the EIT can be found in [38]

1.2.6 Current Patterns

The application of all possible currents is impossible as stated in the inverse problem. In practice, since there are L electrodes, there are at most $L - 1$ linearly independent current patterns. Any other current pattern will be a linear combination of these. Popular choice of the current pattern are:

- i. Trigonometric current patterns: This is modeled as follows:

$$I_l^n = \begin{cases} M \cos(n\theta_l), & n = 1, \dots, \frac{L}{2} - 1, \\ M \cos(\pi l), & n = L/2, \\ M \sin((n - L/2)\theta_l), & n = \frac{L}{2} + 1, \dots, L - 1 \end{cases}$$

where M is the maximum current amplitude. The vector I^n is a discrete approximation to $M \cos(n\theta)$ for $1 \leq n \leq L/2$ or $M \sin(n\theta)$ for $L/2 - 1 \leq n \leq L - 1$

- ii. Pairwise current injection: For a system with a single current source, current patterns that apply equal and opposite current on pairs of electrodes will preserve Kirchhoff's law. It is given by

$$I_l^k = \begin{cases} M, & l = k, k = 1, 2, \dots, L \\ -M, & l = k + 1, k = 1, \dots, L + 1 \\ -M, & l = 1, k = L \\ 0 & \text{otherwise} \end{cases}$$

A detailed discussion of the optimal current patterns and distinguishability in EIT and a description of various current patterns for EIT can be found in [97]

1.3 Numerical solution to the forward EIT problem

A numerical solution to the forward EIT problem of computing the potential u from generalized Laplace equation (1.1) knowing the interior conductivity σ and the boundary condition (1.4) can be accomplished by Finite Element Methods (FEM). Below is a summary of the Finite Element Method applied to forward EIT problem using complete electrode model. The detailed analysis of FEM for CEM and the convergence of solutions is discussed in [97].

Computing DN matrix: Choosing some $N > 0$ and using the truncated Fourier basis functions

$$\varphi_n(\theta) = (2\pi)^{-1/2} e^{in\theta}, \quad n \in \mathbb{Z} \quad (1.16)$$

with $-N \leq n \leq N$, the DN map Λ_σ can be approximated by the $(2N + 1) \times (2N + 1)$ matrix $\mathbf{L}_\sigma = [(\mathbf{L}_\sigma)_{m,n}]$ defined by

$$(\mathbf{L}_\sigma)_{m,n} := \langle \Lambda_\sigma \varphi_n, \varphi_m \rangle = \frac{1}{\sqrt{2\pi}} \int_0^{2\pi} (\Lambda_\sigma \varphi_n) e^{-im\theta} d\theta. \quad (1.17)$$

Variational formulation: Consider the boundary conditions for the complete electrode model.

$$\int_{e_l} \sigma \frac{\partial u}{\partial \nu} ds = I_l, l = 1, 2, \dots, L, \quad (1.18)$$

$$\sigma \frac{\partial u}{\partial \nu} = 0 \quad \text{off} \quad \bigcup_{l=1}^L e_l. \quad (1.19)$$

and Robin boundary condition

$$u + z_l \sigma \frac{\partial u}{\partial \nu} = U_l \quad \text{on } e_l \quad \text{for } l = 1, 2, \dots, L, \quad (1.20)$$

with the choice of ground being specified by the uniqueness condition

$$\sum_{l=1}^L U_l = 0, \quad (1.21)$$

and Kirchoff's law

$$\sum_{l=1}^L I_l = 0. \quad (1.22)$$

where z_l denotes the effective contact impedance between the l electrode and the skin.

Denoting an electrical potential inside Ω by lowercase u or v , and the vectors of voltages measured on L electrodes by uppercase letters, for any (v, V) , the variational form of the complete electrode model is

$$B_s((u, U), (v, V)) = \sum_{l=1}^L I_l \bar{V}_l \quad (1.23)$$

where $v \in H^1(\Omega)$ and $V \in \mathbb{C}^L$ and \bar{V} denotes the complex conjugate of V and the sesquilinear form $B_s : H \times H \rightarrow \mathbb{C}$ is given by

$$B_s((u, U), (v, V)) = \int_{\Omega} \sigma \nabla u \cdot \nabla \bar{v} \, dx \, dy + \sum_{l=1}^L \frac{1}{z_l} \int_{e_l} (u - U_l)(v - \bar{V}_l) \, dS. \quad (1.24)$$

Discretizing the variational problem leads to the Finite Element Formulation. The domain Ω is discretized into small tetrahedral elements with N nodes in the mesh. Suppose (u, U) is a solution to the complete electrode model with trigonometric current patterns, then a finite dimensional approximation to the voltage distribution inside Ω is given by:

$$u^h(z) = \sum_{k=1}^N \alpha_k \varphi_k(z) \quad (1.25)$$

and on electrodes

$$U^h(z) = \sum_{k=N+1}^{N+(L-1)} \beta_{(k-N)} \vec{n}_{(k-n)}, \quad (1.26)$$

where discrete approximation is indicated by h and the basis functions for the finite dimensional space $\mathcal{H} \subset H^1(\Omega)$ is given by φ_k , and α_k and $\beta_{(k-N)}$ are the coefficients to be determined

$$\vec{n}_j = (1, 0, \dots, 0, -1, 0, \dots, 0)^T \in \mathbb{R}^{L \times 1} \quad (1.27)$$

and -1 is in the position of $(j - 1)$ The choice of $\vec{n}_{(k-N)}$ satisfies the condition for ground in (2.47), since $\vec{n}_{(k-N)}$ in (2.53) results in

$$U^h(z) = \left(\sum_{k=1}^{L-1} \beta_k, -\beta_1, \dots, -\beta_{L-1} \right)^T \quad (1.28)$$

In order to implement FEM computationally we need to expand (2.50) using approximating functions (2.52) and (2.53) with $v = \varphi_j$ for $j = 1, 2, \dots, N$ and $V = \vec{n}_j$ for $j = N + 1, N + 2, \dots, N + (L - 1)$ to get a linear system

$$A\vec{b} = \vec{f}, \quad (1.29)$$

where $\vec{b} = (\vec{\alpha}, \vec{\beta})^T \in \mathbb{C}^{N+L-1}$ with the vector $\vec{\alpha} = (\alpha_1, \alpha_2, \dots, \alpha_N)$ and the vector $\vec{\beta} = (\beta_1, \beta_2, \dots, \beta_{L-1})$, and $A \in \mathbb{C}^{(N+L-1)}$ is of the form

$$A = \begin{pmatrix} B & C \\ \tilde{C} & D \end{pmatrix} \quad (1.30)$$

where B, C and D are matrices that are built below.

The right-hand-side vector is given by

$$\vec{f} = (\mathbf{0}, \tilde{I})^T, \quad (1.31)$$

where $\mathbf{0} \in \mathbb{C}^{1 \times N}$ and $\tilde{I} = (I_1 - I_2, I_1 - I_3, \dots, I_1 - I_L) \in \mathbb{C}^{1 \times (L-1)}$. The entries of $\vec{\alpha}$ represent the voltages throughout the domain, while those of $\vec{\beta}$ are used to find the voltages on the electrodes by

$$U^h = \mathcal{C} \vec{\beta} \quad (1.32)$$

where \mathcal{C} is the $L \times (L-1)$ matrix

$$\mathcal{C} = \begin{pmatrix} 1 & 1 & 1 & \dots & 1 \\ -1 & 0 & 0 & \dots & 0 \\ 0 & -1 & 0 & \dots & 0 \\ & & \ddots & & \\ 0 & 0 & 0 & \dots & -1 \end{pmatrix} \quad (1.33)$$

i. The entries of the block matrix B are determined as follows:

For $1 \leq \mathbf{k}, \mathbf{j} \leq \mathbf{N}$. In this case $u^h \neq 0, U^h = 0, v \neq 0$, but $V = 0$. The sesquilinear form can be simplified to

$$B_s((u^h, U^h), (v, V)) := \int_{\Omega} \sigma \nabla u^h \cdot \nabla \bar{v} dx + \sum_{l=1}^L \frac{1}{z_l} \int_{e^l} u^h \bar{v} dS = 0. \quad (1.34)$$

Thus, the (k, j) entry of the block matrix B becomes,

$$B_{kj} = \int_{\Omega} \sigma \nabla \phi_k \cdot \nabla \bar{\phi}_j dx + \sum_{l=1}^L \frac{1}{z_l} \int_{e^l} \phi_k \bar{\phi}_j dS. \quad (1.35)$$

ii. The entries of the block matrix C are determined as follows:

For $1 \leq \mathbf{k} \leq \mathbf{N}, \mathbf{N} + 1 \leq \mathbf{j} \leq \mathbf{N} + (\mathbf{L} - 1)$. In this case $u^h \neq 0, U^h = 0, v = 0$, and $V \neq 0$.

The sesquilinear form simplifies to

$$B_s((u^h, 0), (0, V)) := - \sum_{l=1}^L \frac{1}{z_l} \int_{e^l} u^h \bar{V}_l ds = I_1 - I_{j+1}. \quad (1.36)$$

Therefore, entries of matrix C become,

$$C_{kj} = - \left[\frac{1}{z_l} \int_{e_l} \varphi_k(\vec{n}_j)_l dS \right]. \quad (1.37)$$

iii. The entries of the block matrix \tilde{C} are determined as follows:

For $N \leq k \leq N + (L - 1)$, $1 \leq j \leq N$. Here $u^h = 0, U^h \neq 0, v \neq 0, V = 0$. The expression for sesquilinear is

$$B_s((0, U^h), (v, 0)) := - \sum_{l=1}^L \frac{1}{z_l} \int_{e_l} U^h \bar{v}_l ds = 0. \quad (1.38)$$

Thus the kj th entry of the \tilde{C} is

$$\tilde{C} = - \left[\sum_{l=1}^L \int_{e_l} \bar{\varphi}_j ds - \frac{1}{z_l + 1} \int_{e_{j+1}} \bar{\varphi}_{j+1} ds \right]. \quad (1.39)$$

iv . The entries of the block matrix D are determined as follows:

For $N \leq k, j \leq N + (L - 1)$. Here $u^h = 0, U^h \neq 0, v = 0, V \neq 0$ The sequilinear form is given by

$$B_s((0, U^h), (0, V)) := \sum_{l=1}^L \frac{1}{z_l} \int_{e_l} U^h \bar{V}_l ds = I_1 - I_{j+1}. \quad (1.40)$$

Thus, the entries of matrix D are given by

$$D_{kj} = \begin{cases} \frac{|e_1|}{z_1} + \frac{|e_{j+1}|}{z_{j+1}}, & j = k - N \\ \frac{|e_1|}{z_1}, & j \neq k - N \end{cases} \quad (1.41)$$

Solving (2.56) gives us the coefficients $\beta_{(k-N)}$ required for the voltages U^h on the electrodes.

1.4 Literature Review

1.4.1 Calderón's Problem

The inverse conductivity problem was first posed by Calderón [35] in 1980 in the theoretical form for dimensions 2 and higher. In this paper he posed the question of whether the conductivity distribution σ of a domain could be uniquely determined from the knowledge of the quadratic form of the DN map Q_σ , also known as power map, where Q_σ is defined by

$$Q_\sigma(\phi) = \int_{\Omega} (\sigma \nabla u) \cdot \nabla u dx \quad (1.42)$$

and to calculate σ in terms of Q_σ , if σ can be determined by Q_σ . This problem came to be known as Calderón's problem. In his paper he proved the injectivity of the Fréchet differential of the linearized problem,

$$dQ(\phi)|_\sigma = \int_{\Omega} \delta |\nabla u|^2 dx, \quad (1.43)$$

by assuming $\sigma(x) = 1 + \delta(x)$, i.e., the conductivity is a small perturbation from a constant throughout the domain. This is equivalent to proving the injectivity of the DN map under a linearized assumption.

Most importantly, Calderón's paper describes a set of complex exponential solutions to Laplace's equation,

$$u_1(x) = e^{\pi i(z \cdot x) + \pi(a \cdot x)} \quad u_2(x) = e^{\pi i(z \cdot x) - \pi(a \cdot x)} \quad (1.44)$$

where a and z are vectors in \mathbb{R}^2 such that $|a| = |z|$ and $a \cdot z = 0$. These solutions grow exponentially in some directions and decay exponentially in others. They are also known as Complex Geometrical Optics (CGO) solutions. Calderón uses CGO solutions to show that if (1.43) vanishes for all harmonic u , then $\delta = 0$ and $dQ(\phi)|_{\sigma=1}$ is injective. In addition to this, Calderón provides an explicit method to approximate σ under the linearized assumption. This involves finding a formula for the approximate Fourier transform of δ and then applying an Inverse Fourier transform. This seminal paper however does not fully answer the question of whether DN map is injective or not.

1.4.2 Further developments on inverse conductivity problem

This seminal paper of Calderón opened doors for many more years of further work on the existence and uniqueness of solutions to inverse conductivity problem.

In 1984, R. Kohn and M. Vogelius proved the following [90]: If $\Omega \in C^\infty$ is bounded and if $\sigma \in L^\infty(\bar{\Omega})$, and $\sigma > 0$ in $\bar{\Omega}$, with $\sigma \in C^\infty$ in some neighbourhood of $\partial\Omega$, then the boundary values of conductivity σ could be uniquely determined in dimensions $n \geq 2$, from the knowledge of DN map Λ_σ . In the following year, the same authors extended the results to piecewise real-analytic conductivities. They also proved that the interior values of σ can be determined in the case of layered structure with $\sigma \in C^3(\bar{\Omega})$ [91]. J. Sylvester and G. Uhlmann gave an explicit reconstruction for σ on $\partial\Omega$, when $\sigma \in C^\infty(\bar{\Omega})$ [112]

In the years 1986 and 1987, Sylvester and Uhlmann provided the first global uniqueness theorems showing the injectivity of the DN map. They proved the uniqueness for 2-D near constant isotropic conductivities when $\partial\Omega \in C^\infty$ [113]. The uniqueness results for the general isotropic $\sigma \in C^\infty$ in dimensions $n \geq 3$ followed later in [114]. In 1988, A. Nachman, J. Sylvester and G. Uhlmann extended the results in dimensions $n \geq 3$ to $\sigma \in C^{1,1}(\bar{\Omega})$ [100]. Later, Nachman used CGO solutions in [114] to provide the first general reconstruction procedure [101] and relaxed the boundary smoothness to $\partial\Omega \in C^{1,1}$. These were extended by Alessandrini to Lipschitz domains, which also included anisotropic conductivities [6]

Nachman in 1996, proved the injectivity of 2-D isotropic C^2 conductivities in Lipschitz domains [102]. In this seminal work, CGO solutions are constructed to a Schrödinger equation that is obtained by transforming the conductivity equation. Then nonlinear Fourier analysis is performed for the inverse conductivity problem. Furthermore, Brown and Uhlmann proved the uniqueness results for $\sigma \in C^1(\Omega)$ [33] and extended to non-smooth conductivities $\sigma \in L^\infty(\Omega)$. The same result was obtained by a different approach by Astala and Päiväranta based on CGO solutions [11].

1.4.3 Reconstruction algorithms and computation

The problem of inverse conductivity was motivated by applications to real world situations. The working computational algorithms for the engineering and biomedical applications are continuously sought by researchers. The goal of a reconstruction algorithm is to obtain an approximation to the conductivity σ on the interior of an object using finite number of finite precision noisy boundary measurements. The numerical methods for the inverse conductivity problem fall into five categories.

1. Linearization technique: In these techniques, the boundary data depends linearly on conductivity, since conductivity is assumed to be a small perturbation from a constant or known distribution. The linearized problem is solved using a regularized inversion method. Calderón provided such a method in 1980 [35]. Computational work based on Calderón's method applied to simulated data can be found in [39], and applied to experimental data can be found in [21, 29], and to elliptical domains in [76]. Noniterative Newton methods, based on one step of a Newton-Raphson method, also known as the NOSER algorithm can be found in [40]. Extensions of NOSER and other one-step Newton methods can be found in [23].
2. Iterative Algorithms: One of the popular methods of iterative algorithm involves reformulating inverse problem as regularized least-squares minimization problem [26, 51, 53]. Here a weighted least-squares error functional $F(\sigma)$ is formed, with the assumption that σ minimizes F and hence fits boundary measurements in a least squares sense. The problem is ill-posed and therefore regularized with a Tikhonov type regularization and then solved using multiple iterations of a quasi-Newton method. Algorithms that are based on the minimization of a regularized equation-error functional can be found in [78]. Although these methods provide accurate conductivity, speedy convergence is not guaranteed.
3. Layer Stripping: These methods are based on boundary voltages corresponding to the highest spatial frequency being used to find the conductivity distribution within some thin layer of the boundary. This is used to synthesize the voltages on subsurface close to boundary, by

solving a Riccati type nonlinear differential equation. It can be assumed that the outermost layer is being stripped off the domain, and conductivity of a second thin layer near this new boundary is computed. This process repeats inductively, and the conductivity is found layer by layer from outside in. This method can be found in [90]. The advantages of this method are that it is computationally fast and provides good approximations for boundary conductivities. However, it is highly unstable in the presence of noise and hence unsuitable for experimental data.

4. **Statistical Inversion Method:** Statistical Inversion schemes reformulate the inverse problem into a type of statistical inference, where all the unknowns of the problem are modeled as random variables. Then the posterior probability density distribution of the unknown variables are estimated, from which the estimates of the conductivity can be computed along with associated *a posteriori* uncertainties. Estimates for conductivity can be found by computing the conditional expectation. This is achieved by Markov Chain Monte Carlo sampling method and can be found in [90]. The Bayesian algorithms are computationally expensive.
5. **D-bar Methods:** Regularized D-bar methods are both nonlinear and direct and allow for a true regularization strategy. This makes them noise robust and hence suitable for real-world data. The D-bar methods are a family of methods based on Complex Geometric Optics solution and the method described here is an implementation of the reconstruction method in [102]. The first numerical implementation was done by S. Siltanen, J.L. Mueller, and D. Isaacson in [83], where the authors applied this method to high and low contrast C^∞ radially symmetric conductivities. Later in 2002, the same authors applied the algorithm to noise free simulated chest phantom with elliptical organ boundaries. There has been extensive studies done on this method and it is now used on clinical data.

The outline of D-bar method is as follows. Consider the change of variables

$$q(z) = \frac{\Delta \sqrt{\sigma(z)}}{\sqrt{\sigma(z)}}, \quad \tilde{u}(z) = \sqrt{\sigma(z)}u(z). \quad (1.45)$$

This transforms the generalized Laplace equation (1.1) to the Schrödinger equation

$$-\Delta \tilde{u}(z) + q(z)\tilde{u}(z) = 0 \quad \text{in } \Omega. \quad (1.46)$$

We assume $\sigma \equiv 1$ near the boundary. Then the Schrödinger potential q satisfies $q = 0$ in the same neighbourhood. Let k be a complex frequency parameter, $k = k_1 + ik_2$. Then we wish to find the CGO solutions $\Psi(z, k)$ to the Schrödinger equation

$$-\Delta \Psi(z, k) + q(z)\Psi(z, k) = 0 \quad \text{in } \mathbb{R}^2 \quad (1.47)$$

subject to the asymptotic condition

$$e^{-ikz}\Psi(z, k) - 1 \in W^{1, \tilde{p}}(\mathbb{R}^2), \quad k \in \mathbb{C} \setminus \{0\} \quad \tilde{p} > 2. \quad (1.48)$$

That is, $\Psi(z, k)$ is asymptotic to e^{ikz} as $|z| \rightarrow \infty$. Now, define a bounded function $\mu(z, k)$ by

$$\mu(z, k) := e^{-ikz}\Psi(z, k). \quad (1.49)$$

It is clear that $\mu(z, k) - 1 \in W^{1, \tilde{p}}(\mathbb{R}^2)$. From the Sobolev embedding theorem, $\mu \in L^\infty(\mathbb{R}^2) \cap C(\mathbb{R}^2)$ and μ is asymptotic to 1 as $|z| \rightarrow \infty$.

The D-bar operators are defined by

$$\begin{aligned} \bar{\partial}_z &= \frac{\partial}{\partial \bar{z}} := \frac{1}{2} \left(\frac{\partial}{\partial x} + i \frac{\partial}{\partial y} \right) \\ \partial_z &= \frac{\partial}{\partial z} := \frac{1}{2} \left(\frac{\partial}{\partial x} - i \frac{\partial}{\partial y} \right). \end{aligned}$$

It is clear from the definition of D-bar operator that

$$\Delta = \frac{\partial^2}{\partial x^2} + \frac{\partial^2}{\partial y^2} = \left(\frac{\partial}{\partial x} + i \frac{\partial}{\partial y} \right) \left(\frac{\partial}{\partial x} - i \frac{\partial}{\partial y} \right) = 4\bar{\partial}_z \partial_z. \quad (1.50)$$

Using (1.50) and $\Psi(z, k) = e^{ikz}\mu(z, k)$ in (1.47), we get,

$$\begin{aligned}
q(z)e^{ikz}\mu(z, k) &= \Delta\Psi(z, k) \\
&= 4\partial\bar{\partial}(e^{ikz}\mu(z, k)) \\
&= 4\partial(e^{ikz}\bar{\partial}\mu(z, k)) \\
&= 4(ik e^{ikz}\bar{\partial}\mu(z, k) + e^{ikz}\partial\bar{\partial}\mu(z, k)) \\
&= e^{ikz}(4ik\bar{\partial} + \Delta)\mu(z, k).
\end{aligned}$$

Thus we have,

$$(-\Delta - 4ik\bar{\partial} + q(z))\mu(z, k) = 0. \quad (1.51)$$

Define Faddeev Green's function to be [56]

$$g_k(z) := \frac{1}{(2\pi)^2} \int_{\mathbb{R}^2} \frac{e^{iz \cdot \xi}}{|\xi|^2 + 2k(\xi_1 + i\xi_2)} d\xi, \quad (1.52)$$

where $\xi = (\xi_1, \xi_2) \in \mathbb{R}^2$ and $z \cdot \xi = x\xi_1 + y\xi_2$. It is clear from standard PDE theory that (1.52) is a fundamental solution to (1.51). Defining the Fourier transform \mathcal{F} and its inverse \mathcal{F}^{-1} by

$$(\mathcal{F}f)(\xi) = \hat{f}(\xi) := \int_{\mathbb{R}^2} e^{-iz \cdot \xi} f(z) dz \quad (\mathcal{F}^{-1}\hat{f})(z) = f(z) := \int_{\mathbb{R}^2} e^{iz \cdot \xi} \hat{f}(\xi) d\xi,$$

it is now straightforward to see that a solution to the Lippmann-Schwinger type integral equation

$$\mu - 1 = -g_k * (q\mu) \quad (1.53)$$

is a solution to (1.51). The conductivity can be recovered from $\mu(z, k)$, by substituting $q(z) = \frac{\Delta\sqrt{\sigma}}{\sqrt{\sigma}}$ and taking $k \rightarrow 0$ in (1.51). We get

$$\Delta\mu(z, 0) = \frac{\Delta\sqrt{\sigma(z)}}{\sqrt{\sigma(z)}}\mu(z, 0). \quad (1.54)$$

Using asymptotic condition $\mu(z, 0) - 1 \in W^{1,\tilde{p}}(\mathbb{R}^2)$ and $\sigma(z) \equiv 1$ on $\mathbb{R}^2 \setminus \Omega$, we get,

$$\lim_{k \rightarrow 0} \mu(z, k) = \sqrt{\sigma(z)}, \quad (1.55)$$

and

$$\mu(z, 0) = \sqrt{\sigma(z)} \quad (1.56)$$

is a solution to (1.54).

The steps of the D-bar algorithm are as follows:

Step 1: Consider the input of noisy EIT data Λ_σ and the noise amplitude $\delta > 0$

Step 2. Solve the boundary integral equation

$$\Psi(z, k)|_{\partial\Omega} = e^{ikz}|_{\partial\Omega} - \int_{\partial\Omega} G_k(z - \zeta)(\Lambda_\sigma - \Lambda_1)(\Psi(\zeta, k))ds(\zeta)$$

to get $\Psi|_{\partial\Omega}$.

Step 3. Using $\Psi|_{\partial\Omega}$ compute the scattering transform $\mathbf{t}(k)$ by

$$\mathbf{t}(k) = \int_{\partial\Omega} e^{i\bar{k}z}(\Lambda_\sigma - \Lambda_1)\Psi(z, k)ds(z)$$

Step 4. Use the scattering transform $\mathbf{t}(k)$ to solve the Fredholm integral equation

$$\mu(z, k) = 1 + \frac{1}{4\pi^2} \int_{\mathbb{R}^2} \frac{\mathbf{t}(k')}{(k - k')k'} e^{-i(k'z + \bar{k}'z)} \overline{\mu(z, k')} dk' \quad (1.57)$$

for $\mu(z, k)$

Step 5: From $\mu(z, k)$ compute $\sigma(z)$ using (1.56)

The details of D-bar method, both theoretical and numerical implementation, can be found in [97].

Chapter 2

Anisotropic inverse conductivity problem

2.1 Introduction

The inverse conductivity problem, that is, given the boundary measurements,

$$\Lambda_\sigma : u|_{\partial\Omega} \rightarrow \sigma \frac{\partial u}{\partial \nu} \Big|_{\partial\Omega} \quad (2.1)$$

to determine the interior conductivity from the generalized Laplace equation,

$$\nabla \cdot (\sigma \nabla u) = 0 \quad (2.2)$$

thus far, has been studied extensively under the assumption that the conductivity σ is isotropic. However, physical properties such as conductivity are dependent on the direction of measurement and hence are anisotropic. The electrical conductivity of certain human tissues such as bones, muscles and brain matter is highly anisotropic in nature. The most striking case is that of skeletal muscle for which the longitudinal conductivity is 15 times more than that of the transversal. Below is a table of electrical conductivities perpendicular and parallel to the pial surface, that is the surface representing the boundary between grey matter and cerebrospinal fluid of neocortex and subcortical matter from pediatric epilepsy surgery patients.

Modeling conductivity as anisotropic may also provide a way to account for out-of-plane currents in either 2-D or 3-D models. We conjecture it may also provide a way to account for inaccuracies in domain shape such as the changes in chest shape caused by breathing. Thus, the study of anisotropic inverse conductivity problem is of practical importance.

The Table 2.1 below emphasizes the difference in the conductivity values that are perpendicular and parallel to the directions of the surface representing the boundary between grey matter and

cerebrospinal fluid, the pial surface of neocortex for various clinical variables. The data is obtained from pediatric epilepsy surgery patients.

Table 2.1: Conductivities in perpendicular and parallel directions on the pial surface of neocortex. (Source: [4])

| Clinical variable | Conductivity perpendicular (mS/cm) | Conductivity parallel(ms/cm) |
|-------------------|------------------------------------|------------------------------|
| Lateral position | 0.077 | 0.701 |
| Gender | 0.389 | 0.899 |
| Seizure onset | 0.788 | 0.986 |
| Epilepsy Duration | 0.788 | 0.161 |
| Seizure frequency | 0.573 | 0.796 |

2.2 Mathematical model of the anisotropic EIT problem

The mathematical model for an anisotropic conductivity EIT problem is as follows: If $\Omega \subset \mathbb{R}^2$ is a simply connected domain, the conductivity is $\sigma = [\sigma^{jk}]$ where $j, k = 1, 2$, is a symmetric, positive definite matrix function, and $\phi \in H^{1/2}(\partial\Omega)$ is the voltage on the boundary. We wish to recover the conductivity σ from the generalized Laplace equation,

$$\nabla \cdot \sigma \nabla u = \sum_{j,k=1}^2 \frac{\partial}{\partial x^j} (\sigma^{jk}(x) \frac{\partial}{\partial x^k} u) = 0 \quad \text{in } \Omega \quad (2.3)$$

$$u|_{\partial\Omega} = \phi \quad (2.4)$$

When σ and $\partial\Omega$ are smooth, the Dirichlet to Neumann map is well defined and given by

$$\Lambda_\sigma(\phi) = Bu|_{\partial\Omega}, \quad (2.5)$$

where

$$Bu = \nu \cdot \sigma \nabla u = \sum_{j,k=1}^2 \sigma^{jk}(x, y) \frac{\partial u}{\partial x_j} \nu_k|_{\partial\Omega}, \quad (2.6)$$

$u \in H^1(\Omega)$ is a solution of (2.3), and ν is the unit outer normal vector of $\partial\Omega$. Using the divergence theorem,

$$Q_{\sigma,\Omega}(\phi) := \int_{\Omega} \sum_{j,k=1}^2 \sigma^{jk}(x) \frac{\partial u}{\partial x^j} \frac{\partial u}{\partial x^k} dx = \int_{\partial\Omega} \Lambda_{\sigma}(\phi) \phi dS \quad (2.7)$$

where dS denotes the arc length on $\partial\Omega$. The quantity $Q_{\sigma,\Omega}$ represents the power needed to maintain the potential ϕ on $\partial\Omega$. By the symmetry of Λ_{σ} , having a knowledge of $Q_{\sigma,\Omega}$ is equivalent to knowing Λ_{σ} .

2.3 Difficulties of anisotropic inverse conductivity problem

2.3.1 History of the problem

The anisotropic inverse conductivity problem was first studied by Kohn and Vogelius in 1983 [91]. In this paper they proved that it is impossible to recover the full matrix σ^{ij} from the boundary value measurements. Ever since, the nonuniqueness of the anisotropic problem has been well established [112].

The non-uniqueness of the anisotropy problem can be explained as follows: [73]

If $F : \Omega \rightarrow \Omega$, $F(x) = (F^1(x), F^2(x))$ is a diffeomorphism with $F|_{\partial\Omega} = Id$, then by making the change of variables $y = F(x)$ and setting $v = u \circ F^{-1}$ in the first integral in (2.7), we get

$$\nabla \cdot (F_*\sigma)\nabla v = 0 \quad \text{in} \quad \Omega, \quad (2.8)$$

where

$$(F_*\sigma)^{jk}(y) = \frac{1}{\det\left[\frac{\partial F^j}{\partial x^k}\right]} \sum_{p,q=1}^2 \frac{\partial F^j}{\partial x^p}(x) \frac{\partial F^k}{\partial x^q}(x) \sigma^{pq}(x) \Bigg|_{x=F^{-1}(y)} \quad (2.9)$$

That is,

$$F_*\sigma(y) = \frac{1}{\det\left[\frac{\partial F^j}{\partial x^k}\right]} DF(x)\sigma(x)DF(x)^T \Bigg|_{x=F^{-1}(y)} \quad (2.10)$$

is the push forward conductivity of σ by F . Since F is the identity on $\partial\Omega$, from (2.7), we get,

$$\Lambda_{F_*\sigma} = \Lambda_{\sigma} \quad (2.11)$$

Therefore, from the change of coordinates, it is evident that a large class of conductivities results in the same electrical measurements at the boundary [73]

2.3.2 Further developments in anisotropic inverse conductivity problem

Despite the issue of nonuniqueness in the anisotropic inverse conductivity problem, researchers world-wide continue to work on it due to its real world applications. Lionheart in 1997 proved the uniqueness result under two different hypothesis. The first of these results relies on the conductivity being determined by boundary measurements up to a diffeomorphism fixing points on the boundary, which has been shown for analytic conductivities to be a constant. The apparatus of G-structures is then used to show that the conformal mapping of a Riemannian manifold that fixes all the points on the boundary must be identity. The second approach is an extension to the piecewise analytic conductivity [96]. In the year 2001, Alessandrini et al proved the uniqueness and stability results for the anisotropic conductivity of the form $A = A(x, a(x))$, where $a(x)$ is an unknown scalar function [8]. In the same paper, the uniqueness result for the interior conductivities of A were also proved by piecewise analytic perturbations of the scalar term a .

There have been a number of theoretical developments on this problem. Lee and Uhlmann, in the year 1984, studied this problem extensively, giving a symbol of the DN map and constructing the diffeomorphism for anisotropic problem [95]. In 2004, Astala et al studied the problem for $\sigma \in L^\infty$ in bounded and unbounded domains and the results were applied in the case when only partial data on the boundary were known [11]. In the year 2008, Takuwa et al constructed complex geometrical optics solutions with general phase functions for the second order elliptic equation in two dimensions [115].

In the year 2011, Abascal et al [1] showed numerically that the uniqueness can be restored by providing information about diffeomorphism. In this paper they were able to show the uniqueness results numerically for two constraints. First, having the knowledge of one eigenvalue and multiple scalar of a general tensor. In the field of medical imaging this can correspond to having *a priori* knowledge from MRI about the eigenvectors, even when eigenvalues are unknown. This opens

up a new door of solving the anisotropic EIT problem in conjunction with other imaging modalities such as MRI or ultrasound.

In 2014 Hamilton et al proposed a reconstruction method for the anisotropic problem [76]. In this paper, the anisotropic DN map is first transformed into anisotropic CGO traces, from which Beltrami scattering data is obtained. This is then used to obtain Schrödinger scattering data, which transforms the problem in to isotropic inverse conductivity problem for which numerical solutions are readily available.

2.4 Injectivity for the linearized anisotropic inverse conductivity problem based on Calderón's method

Let $\Omega \subset \mathbb{R}^2$ be a simply connected domain with Lipschitz boundary $\partial\Omega$, and conductivity $\sigma = (\sigma^{jk})_{j,k=1,2}$ is a symmetric positive definite matrix function. Consider the second order differential elliptic operator

$$L_\sigma \cdot = \nabla \cdot (\sigma \nabla \cdot) \quad (2.12)$$

acting on functions of $H^1(\Omega)$ (in the weak sense). The quadratic form $Q_{\sigma,\Omega}(\phi)$, where the function $\phi \in H^{1/2}(\partial\Omega)$ is the voltage on the boundary is given by

$$Q_{\sigma,\Omega}(\phi) := \int_{\Omega} \sum_{j,k=1}^2 \sigma^{jk}(x) \frac{\partial u}{\partial x^j} \frac{\partial u}{\partial x^k} dx = \int_{\partial\Omega} \Lambda_\sigma(\phi) \phi dS. \quad (2.13)$$

The problem of anisotropic EIT is to determine whether σ is uniquely determined by the quadratic form $Q_{\sigma,\Omega}$ and if it is so, then to calculate σ in terms of $Q_{\sigma,\Omega}$. In order to determine conductivity σ , we impose the following conditions on σ .

- i. The conductivity σ is a positive definite matrix, i.e., there exists a universal constant $\lambda \in (0, 1)$ such that

$$\lambda |\xi|^2 \leq \sum_{j,k=1}^2 \sigma^{jk}(x) \xi_j \xi_k \leq \lambda^{-1} |\xi|^2, \text{ for all } x \in \Omega \text{ and } \xi \in \mathbb{R}^2.$$

- ii. The conductivity is assumed to be of the form $\sigma = a(x)A_0$, where $a(x)$ is a scalar function to be determined and A_0 is the known constant 2×2 positive definite anisotropic tensor.

Let us introduce the norms in the space of σ and in the space of quadratic forms $Q_\sigma \equiv Q_{\sigma,\Omega}(\phi)$ as follows:

$$\|\phi\|^2 := \int_{\Omega} |\nabla u|^2 dx, \quad (2.14)$$

where $u \in H^1(\Omega)$ is a solution of the following constant second order elliptic equation

$$\nabla \cdot (A_0 \nabla u) = 0 \text{ in } \Omega, \text{ with } u|_{\partial\Omega} = \phi \text{ on } \partial\Omega, \quad (2.15)$$

and

$$\|Q_\sigma\| = \sup_{\|\phi\| \leq 1} |Q_\sigma(\phi)|. \quad (2.16)$$

Analyticity of Φ in the case that follow from the argument outlined below. Here Φ is given by

$$\Phi : \sigma \rightarrow Q_\sigma \quad (2.17)$$

σ is a perturbation from A_0 given by $\sigma := A = A_0 + \delta(x)A_0$. Let u be the solution to the PDE

$$L_A(u) = \nabla \cdot (A \nabla u) = 0; \quad u|_{\partial\Omega} = \phi. \quad (2.18)$$

Let $w = u + v$, where $L_{A_0}u = 0$, $u|_{\partial\Omega} = \phi$. Then,

$$L_A(w) = L_{A_0+\delta(x)A_0}(u + v) = L_{A_0}v + L_{\delta A_0}v + L_{\delta A_0}u = 0, \quad (2.19)$$

and $v|_{\partial\Omega} = 0$.

Lemma 1. *The operator L_{A_0} has a bounded inverse operator G and v has the following H^1 bound*

$$\|v\|_{H^1(\Omega)} \leq \frac{\|G\| \|\delta\|_\infty \|A_0\| \|\phi\|}{1 - \|G\| \|\delta\|_\infty \|A_0\|}, \quad (2.20)$$

where $\|G\| := \|G\|_{\mathcal{L}(H^{-1};H^1)}$ denotes the operator norm from H^{-1} to H^1 , $\|A_0\|$ stands for the Frobenius norm of the constant matrix A_0 , and $\|\phi\|$ is given by (2.14).

Proof. Since $L_{A_0}u = 0$, $u|_{\partial\Omega} = \phi$ has a unique solution u , the operator L_{A_0} has a bounded inverse G .

Then from (2.19) we get,

$$G(L_{A_0}v + L_{\delta A_0}v + L_{\delta A_0}u) = 0. \quad (2.21)$$

That is

$$(I + GL_{\delta A_0})v = -GL_{\delta A_0}u. \quad (2.22)$$

We note that

$$\|L_{\delta A_0}w\|_{H^{-1}(\Omega)} = \sup_{\psi \in H_0^1(\Omega)} \frac{|\int_{\Omega} \nabla \cdot [(\delta(x)A_0)\nabla w]\psi dx|}{\|\psi\|_{H_0^1(\Omega)}}, \quad (2.23)$$

and

$$\begin{aligned} \left| \int_{\Omega} \nabla \cdot [(\delta(x)A_0)\nabla w]\psi dx \right| &= \left| \int_{\Omega} \nabla \psi \cdot [(\delta(x)A_0)\nabla w] dx \right| \\ &\leq \|\delta(x)A_0\|_{L^\infty(\Omega)} \|\nabla w\|_{L^2(\Omega)} \|\psi\|_{H_0^1(\Omega)}. \end{aligned} \quad (2.24)$$

Thus, from (2.23) and (2.24), we get

$$\|L_{\delta A_0}w\|_{H^{-1}(\Omega)} \leq \|\delta(x)A_0\|_{L^\infty(\Omega)} \|\nabla w\|_{L^2(\Omega)}. \quad (2.25)$$

Next, consider the operator norm

$$\|GL_{\delta A_0}\|_{\mathcal{L}(H^1;H^1)} = \sup_{w \neq 0} \frac{\|GL_{\delta A_0}w\|_{H^1(\Omega)}}{\|w\|_{H^1(\Omega)}} \leq \frac{\|G\|_{\mathcal{L}(H^{-1};H^1)} \|L_{\delta(x)A_0}w\|_{H^{-1}(\Omega)}}{\|w\|_{H^1(\Omega)}}, \quad (2.26)$$

where $\|\cdot\|_{\mathcal{L}(X;Y)}$ stands for the operator norm from two Banach spaces X to Y . That is,

$$\|GL_{\delta A_0}\|_{\mathcal{L}(H^1;H^1)} \leq \|G\|_{\mathcal{L}(H^{-1};H^1)} \|\delta A_0\|_{L^\infty(\Omega)} \quad (2.27)$$

When $\|\delta(x)A_0\|_{L^\infty(\Omega)} < \frac{1}{\|G\|_{\mathcal{L}(H^{-1};H^1)}}$, the Neumann series

$$\left[\sum_{j=0}^{\infty} (-1)^j (GL_{\delta A_0})^j \right] (GL_{\delta A_0} u)$$

converges, and from (2.22), then one has

$$v = - \left[\sum_{j=0}^{\infty} (-1)^j (GL_{\delta A_0})^j \right] (GL_{\delta A_0} u). \quad (2.28)$$

It is easy to see that

$$\begin{aligned} \|v + GL_{\delta A_0} v\|_{H^1(\Omega)} &\geq \|v\|_{H^1(\Omega)} - \|GL_{\delta A_0} v\|_{H^1(\Omega)} \\ &\geq \|v\|_{H^1(\Omega)} (1 - \|G\|_{\mathcal{L}(H^{-1};H^1)} \|\delta(x)A_0\|_{L^\infty(\Omega)}). \end{aligned} \quad (2.29)$$

Finally, by using relations (2.21) and (2.25),

$$\begin{aligned} (1 - \|G\|_{\mathcal{L}(H^{-1};H^1)} \|\delta(x)A_0\|_{L^\infty(\Omega)}) \|v\|_{H^1(\Omega)} &\leq \|v + G(-L_{\delta A_0} u - L_{A_0} v)\|_{H^1(\Omega)} \\ &= \|v - GL_{\delta A_0} u - v\|_{H^1(\Omega)} \\ &\leq \|G\|_{\mathcal{L}(H^{-1};H^1)} \|L_{\delta A_0} u\|_{H^{-1}(\Omega)} \\ &= \|G\|_{\mathcal{L}(H^{-1};H^1)} \|\delta(x)A_0\|_{L^\infty(\Omega)} \|\phi\|, \end{aligned}$$

and substituting (2.29) into the above inequality results in

$$\|v\|_{H^1(\Omega)} \leq \frac{\|G\|_{\mathcal{L}(H^{-1};H^1)} \|\delta(x)A_0\|_{L^\infty(\Omega)} \|\phi\|}{1 - \|G\|_{\mathcal{L}(H^{-1};H^1)} \|\delta(x)A_0\|_{L^\infty(\Omega)}}. \quad (2.30)$$

Therefore, the above calculations allow us to conclude that the mapping Φ (2.17) is analytic at A_0 , which completes the proof. \square

Next, linearize the map $Q_A(\phi)$ about a positive definite matrix $A = A_0$ to get

$$\begin{aligned}
Q_{A_0+\delta(x)A_0}(\phi) &= \int_{\Omega} [(A_0 + \delta(x)A_0)\nabla w] \cdot \nabla w dx \\
&= \int_{\Omega} [(A_0 + \delta(x)A_0)\nabla u] \cdot \nabla u dx + 2 \int_{\Omega} (\delta(x)A_0\nabla u) \cdot \nabla v dx \\
&\quad + \int_{\Omega} [(A_0 + \delta(x)A_0)\nabla v] \cdot \nabla v dx,
\end{aligned} \tag{2.31}$$

where we have used that $\nabla \cdot (A_0\nabla u) = 0$ in Ω . We now show that $\int_{\Omega} (\delta(x)A_0\nabla u) \cdot \nabla v dx$ and $\int_{\Omega} [(A_0 + \delta(x)A_0)\nabla v] \cdot \nabla v dx$ are of $o(\|\delta\|)$. It is easy to see that

$$\left| \int_{\Omega} (\delta(x)A_0)\nabla u \cdot \nabla v dx \right| \leq C_{A_0} \|\delta\|_{L^\infty(\Omega)} \|\phi\| \|v\|_{H^1(\Omega)}, \tag{2.32}$$

and

$$\left| \int_{\Omega} [(A_0 + \delta(x)A_0)\nabla v] \cdot \nabla v dx \right| \leq C_{A_0} (1 + \|\delta\|_{L^\infty(\Omega)}) \|v\|_{H^1(\Omega)}^2, \tag{2.33}$$

for some constant $C_{A_0} > 0$ independent of δ . By inserting (2.30) into (2.32), (2.33) and taking $\|\delta\|_{L^\infty(\Omega)}$ sufficiently small, one obtains the desired result. Thus, the Fréchet derivative of $Q_A(\phi)$ at $A(x) = A_0$ is given by

$$dQ_A(\phi) \Big|_{A=A_0} = \int_{\Omega} ((\delta(x)A_0)\nabla u) \cdot \nabla u dx, \tag{2.34}$$

where $u \in H^1(\Omega)$ is a solution of $\nabla \cdot (A_0\nabla u) = 0$ in Ω with $u = \phi$ on $\partial\Omega$.

Theorem 1. *The Fréchet derivative $dQ_A(\phi) \Big|_{A=A_0}$ is injective.*

In order to prove the above theorem, we utilize the famous quasi-conformal map in the plane, which can be found in [11, 115].

Lemma 2 (Quasi-conformal map). *Given any 2×2 matrix A , there exists a quasi-conformal map $\Phi^{(A)} : \mathbb{C} \rightarrow \mathbb{C}$ such that $\Phi^{(A)} \in W^{1,p}(\mathbb{C}; \mathbb{C})$ for some $p > 2$ with*

$$\Phi^{(A)}(z) = z + O\left(\frac{1}{z}\right) \quad \text{as } z \rightarrow \infty,$$

with

$$\Phi_*^{(A)}A(z) = \sqrt{\det(A((\Phi^{(A)})^{-1}(z)))}I_2,$$

where I_2 is the 2×2 identity matrix and

$$\Phi_*^{(A)}A(y) = \frac{\nabla(\Phi^{(A)})(x)A(x)\nabla(\Phi^{(A)})^T(x)}{\det(\nabla(\Phi^{(A)})(x))}\Big|_{x=(\Phi^{(A)})^{-1}(y)}, \quad (2.35)$$

with

$$(\Phi_*^{(A)}A)^{i\ell}(y) := \frac{1}{\det(\nabla(\Phi^{(A)}))} \sum_{j,k=1}^2 \partial_{x^j}(\Phi^{(A)})^i(x) \partial_{x^k}(\Phi^{(A)})^\ell(x) A^{jk}(x) \Big|_{x=(\Phi^{(A)})^{-1}(y)}.$$

Furthermore, $\Phi^{(A)}$ solves the following Beltrami equation

$$\bar{\partial}_z \Phi^{(A)} = \mu_A \partial_z \Phi^{(A)},$$

where

$$\mu_A = \frac{A^{22} - A^{11} - 2iA^{12}}{A^{11} + A^{22} + 2\sqrt{\det A}}. \quad (2.36)$$

Proof. In order to prove that $dQ_A(\phi)|_{A=A_0}$ is injective, we only need to show that

$$\int_{\Omega} (\delta(x)A_0 \nabla u) \cdot \nabla u \, dx = 0 \text{ implies that } \delta \equiv 0,$$

where $u \in H^1(\Omega)$ is a solution of $L_{A_0}u = 0$ in Ω with $u = \phi$ on $\partial\Omega$. On the other hand, since the last integral in (2.34) vanishes for all such u , then it is equivalent to prove

$$\int_{\Omega} ((\delta(x)A_0)\nabla u_1) \cdot \nabla u_2 \, dx = 0, \quad (2.37)$$

where $u_1, u_2 \in H^1(\Omega)$ are solutions of $L_{A_0}u_1 = L_{A_0}u_2 = 0$ in Ω . Inspired by [35], we want to find special exponential solutions to achieve our goal.

From Lemma 2, given an anisotropic conductivity $A(x)$, it is known that there exists a C^1 bijective map $\Phi^{(A)} : \mathbb{R}^2 \rightarrow \mathbb{R}^2$ with $y = \Phi^{(A)}(x)$ such that

$$\Phi_*^{(A)} A = (\det A \circ (\Phi^{(A)})^{-1})^{1/2} I_2, \quad (2.38)$$

is equivalent to a scalar conductivity. Moreover, $\Phi^{(A)}$ solves the following Beltrami equation in the complex plane \mathbb{C} ,

$$\bar{\partial}\Phi^{(A)} = \mu_A \partial\Phi^{(A)},$$

where μ_A is given by (2.36) and

$$\bar{\partial} = \frac{1}{2}(\partial_{x_1} + i\partial_{x_2}), \quad \partial = \frac{1}{2}(\partial_{x_1} - i\partial_{x_2}).$$

Next, from the representation (2.38) and (2.35), we know that there exists a quasi-conformal map $\Phi^{(A_0)}$ such that

$$\tilde{A}_0 := \Phi_*^{(A_0)} A_0 = \frac{\nabla\Phi^{(A_0)}(x) A_0 \nabla(\Phi^{(A_0)})^T(x)}{\det(\nabla\Phi^{(A_0)}(x))} \Big|_{x=(\Phi^{(A_0)})^{-1}(y)} = \sqrt{\det A_0} I_2 \quad (2.39)$$

with $\det A_0 > 0$. Note that $\delta = \delta(x)$ is a scalar function, then by using the formula (2.35) and (2.39), one can see that

$$\begin{aligned} \Phi_*^{(A_0)}(\delta(x)A_0) &= \frac{\nabla\Phi^{(A_0)}(x) (\delta(x)A_0) \nabla(\Phi^{(A_0)})^T(x)}{\det(\nabla\Phi^{(A_0)}(x))} \Big|_{x=(\Phi^{(A_0)})^{-1}(y)} \\ &= \delta(x) \Big|_{x=(\Phi^{(A_0)})^{-1}(y)} \sqrt{\det A_0} I_2. \end{aligned}$$

Let $\Phi \equiv \Phi^{(A_0)}$, $\tilde{\Omega} := \Phi(\Omega)$ and $\tilde{u}_j(y) := u_j \circ (\Phi^{-1}(y))$ for $j = 1, 2$, by using (2.37) and change of variables $y = \Phi(x)$ via the quasi-conformal map, then we obtain that

$$\int_{\tilde{\Omega}} \Phi_*(\delta(x)A_0) \nabla_y \tilde{u}_1 \cdot \nabla_y \tilde{u}_2 dy = \int_{\Omega} ((\delta(x)A_0) \nabla u_1) \cdot \nabla u_2 dx = 0, \quad (2.40)$$

where \tilde{u}_j are solutions of

$$L_{\tilde{A}_0} \tilde{u}_1 = L_{\tilde{A}_0} \tilde{u}_2 = 0 \text{ in } \tilde{\Omega}. \quad (2.41)$$

As a matter of fact, (2.41) is equivalent to the Laplace equation $\Delta_y \tilde{u}_j = 0$ in $\tilde{\Omega}$ for $j = 1, 2$ because $\tilde{A}_0 = \sqrt{\det A_0} I_2$ with $\det A_0$ being a positive constant. Based on Calderón's constructions [?], we can consider two special exponential solutions as follows. Let $\xi \in \mathbb{R}^2$ be an arbitrary vector and $a \in \mathbb{R}^2$ such that $\xi \cdot a = 0$ and $|\xi| = |a|$, then one can choose

$$\tilde{u}_1(y) := e^{\pi i(\xi \cdot y) + \pi(a \cdot y)} \quad \text{and} \quad \tilde{u}_2(y) := e^{\pi i(\xi \cdot y) - \pi(a \cdot y)}, \quad (2.42)$$

and it is easy to check that \tilde{u}_1 and \tilde{u}_2 are solutions of the Laplace equation. By plugging these exponential solutions (2.42) into (2.40), one has

$$2\pi|\xi|^2 \int_{\tilde{\Omega}} (\delta \circ \Phi^{-1}(y)) \sqrt{\det A_0} e^{2\pi \xi \cdot y} dy = 0, \text{ for any } \xi \in \mathbb{R}^2,$$

which implies that $\delta = 0$, due to the positivity of $\det A_0$. This accomplishes the proof. □

It is worth mentioning that

- i. Due to the remarkable quasi-conformal map in the plane, one can reduce the anisotropic conductivity equation into an isotropic one. This method helps us to develop the reconstruction algorithm for the anisotropic conductivity equation proposed by Calderón.
- ii. The method fails when the space dimension $n \geq 3$, because there are no suitable CGO solutions for the anisotropic case.

2.5 Bayesian formulation of the anisotropic EIT problem

Due to the non-uniqueness of the anisotropic inverse conductivity problem, we need to include additional information in the reconstruction algorithm, that is, we need a prior. Our prior is the knowledge of the tensor of anisotropy. This can be easily obtained for the problem with the help of another imaging modality such as DT-MRI. With this prior knowledge we want to explore the Bayesian framework. The Bayesian framework provides a way to include prior information in the penalty term with a bit more flexibility than traditional least squares regularization and some quantification on the certainty of the chosen conductivity estimation as well as a set of possible solutions. The use of the Bayesian framework has not yet been investigated for the anisotropic problem in EIT and provides a natural way to incorporate priors, which is essential to obtain uniqueness in the anisotropic inverse conductivity problem. The application of the Bayesian framework to the EIT problem in the case of isotropic conductivity is explained in detail in [36].

The Bayesian framework is well suited for imaging problems, since it allows the utilization of qualitative information about the image to be recovered. In the Bayesian approach the solution to the imaging problem is a distribution of images as opposed to single image, and it is possible to analyze the uncertainties due to measurement errors and to explicitly stated beliefs. The Bayesian solution is a probability density function for the unknown of primary interest, which is built from the *a priori* beliefs about the solution and the likelihood, which in turn encodes the information carried by the available data [37, 86]. In the Bayesian approach, randomness of the unknown is not a property of that is to be recovered, but an expression of the lack of information about it. From this perspective, the prior is not intended to be representative of the unknown, but rather of our belief about it without considering the data, which can be either reinforced or contrasted by the data via the likelihood. Thus, the posterior density is the result of the synthesis of the prior belief and the information carried by data, and as such reflects the relative strengths of the prior and likelihood.

2.6 Forward anisotropic EIT problem

To implement the Bayesian approach to the anisotropic EIT problem, we first need to compute the forward solution. The physical setup for the EIT problem consists of L electrodes attached on the surface $\partial\Omega$ of the body. The electrodes are modeled as surface patches and denoted by $e_l \in \partial\Omega$. A current I_l is injected through each electrode e_l . The vector $I = [I_1, I_2, \dots, I_L]^T$ is a current pattern. The forward problem is to compute u , the electric potential in Ω given by the generalized Laplace equation

$$\nabla \cdot (\sigma \nabla u) = \sum_{j,k=1}^2 \frac{\partial}{\partial x^j} (\sigma^{jk}(x, y) \frac{\partial}{\partial x^k} u) = 0, \quad (x, y) \in \Omega \quad (2.43)$$

subject to the boundary conditions

$$\int_{e_l} \sum_{j,k=1}^2 \sigma^{jk} \frac{\partial u}{\partial x^j} ds = I_l, \quad l = 1, 2, \dots, L, \quad (2.44)$$

$$\sum_{j,k=1}^2 \sigma^{jk} \frac{\partial u}{\partial x^j} = 0 \quad \text{off} \quad \bigcup_{l=1}^L e_l. \quad (2.45)$$

and Robin Boundary condition

$$u + z_l \sum_{j,k=1}^2 \sigma^{jk} \frac{\partial u}{\partial x^j} = U_l \quad \text{on} \quad e_l \quad \text{for} \quad l = 1, 2, \dots, L, \quad (2.46)$$

with the choice of ground being specified by uniqueness condition

$$\sum_{l=1}^L U_l = 0, \quad (2.47)$$

and Kirchoff's law

$$\sum_{l=1}^L I_l = 0. \quad (2.48)$$

where z_l denotes the effective contact impedance between the l th electrode and the skin.

2.6.1 Variational formulation of the anisotropic EIT

Let ϕ_i be piecewise linear shape basis functions defined on a triangular mesh such that $\phi_i = 1$ at the i th node and zero at the other nodes. Here $i = 1, 2, \dots, N$ are the number of vertices in the mesh. Conductivity and voltage are expressed in terms of ϕ_i as

$$u = \sum_{j=1}^N u_j \phi_j \quad \text{and} \quad \sigma = \sum_{i=1}^N \sigma_i \phi_i. \quad (2.49)$$

Denoting an electrical potential inside Ω by lowercase u or v , and the vectors of voltages measured on L electrodes by uppercase letters, for any (v, V) , the variational form of the complete electrode model is

$$B_s((u, U), (v, V)) = \sum_{l=1}^L I_l V_l \quad (2.50)$$

where $v \in H^1(\Omega)$, $V \in \mathbb{R}^L$ and the sesquilinear form $B_s : H \times H \rightarrow \mathbb{R}$ is given by

$$B_s((u, U), (v, V)) = \int_{\Omega} \sigma \nabla u \cdot \nabla v \, dx \, dy + \sum_{l=1}^L \frac{1}{z_l} \int_{e_l} (u - U_l)(v - V_l) dS. \quad (2.51)$$

2.6.2 Finite Element Formulation of anisotropic EIT

Discretizing the variational problem leads to the Finite Element Formulation. The domain Ω is discretized into small tetrahedral elements with N nodes in the mesh. Suppose (u, U) is a solution to the complete electrode model with skip 0 current patterns, then a finite dimensional approximation to the voltage distribution inside Ω is given by:

$$u^h(z) = \sum_{k=1}^N \alpha_k \phi_k(z) \quad (2.52)$$

and on electrodes

$$U^h(z) = \sum_{k=N+1}^{N+(L-1)} \beta_{(k-N)} \vec{n}_{(k-n)}, \quad (2.53)$$

where discrete approximation is indicated by h and the basis functions for the finite dimensional space $\mathcal{H} \subset H^1(\Omega)$ is given by ϕ_k , and α_k and $\beta_{(k-N)}$ are the coefficients to be determined. Let

$$\vec{n}_j = (1, 0, \dots, 0, -1, 0, \dots, 0)^T \in \mathbb{R}^{L \times 1} \quad (2.54)$$

and -1 is in the position of $(j - 1)$. The choice of $\vec{n}_{(k-N)}$ satisfies the condition for ground in (2.47), since $\vec{n}_{(k-N)}$ in (2.53) results in

$$U^h(z) = \left(\sum_{k=1}^{L-1} \beta_k, -\beta_1, \dots, -\beta_{L-1} \right)^T \quad (2.55)$$

In order to implement FEM computationally we need to expand (2.50) using approximating functions (2.52) and (2.53) with $v = \phi_j$ for $j = 1, 2, \dots, N$ and $V = \vec{n}_j$ for $j = N + 1, N + 2, \dots, N + (L - 1)$ to get a linear system

$$A\vec{b} = \vec{f}, \quad (2.56)$$

where $\vec{b} = (\vec{\alpha}, \vec{\beta})^T \in \mathbb{R}^{N+L-1}$ with the vector $\vec{\alpha} = (\alpha_1, \alpha_2, \dots, \alpha_N)$ and the vector $\vec{\beta} = (\beta_1, \beta_2, \dots, \beta_{L-1})$, and $A \in \mathbb{A}^{(N+L-1)}$ is of the form

$$A = \begin{pmatrix} B & C \\ \tilde{C} & D \end{pmatrix}. \quad (2.57)$$

The right-hand-side vector is given by

$$\vec{f} = (\mathbf{0}, \tilde{I})^T, \quad (2.58)$$

where $\mathbf{0} \in \mathbb{R}^{1 \times N}$ and $\tilde{I} = (I_1 - I_2, I_1 - I_3, \dots, I_1 - I_L) \in \mathbb{R}^{1 \times (L-1)}$. The entries of $\vec{\alpha}$ represent the voltages throughout the domain, while those of $\vec{\beta}$ are used to find the voltages on the electrodes by

$$U^h = \mathcal{C} \vec{\beta} \quad (2.59)$$

where \mathcal{C} is the $L \times (L - 1)$ matrix, given by

$$\mathcal{C} = \begin{pmatrix} 1 & 1 & 1 & \dots & 1 \\ -1 & 0 & 0 & \dots & 0 \\ 0 & -1 & 0 & \dots & 0 \\ & & \ddots & & \\ 0 & 0 & 0 & \dots & -1 \end{pmatrix}. \quad (2.60)$$

The entries of the block matrix A are determined as follows:

- i. For $1 \leq \mathbf{k}, \mathbf{j} \leq \mathbf{N}$. In this case $u^h \neq 0, U^h = 0, v \neq 0$, but $V = 0$. The sesquilinear form can be simplified to

$$B_s((u^h, U^h), (v, V)) := \int_{\Omega} \sigma \nabla u^h \cdot \nabla v dx + \sum_{l=1}^L \frac{1}{z_l} \int_{e^l} u^h v dS = 0 \quad (2.61)$$

Thus, the (k, j) th entry of the block matrix B becomes,

$$B_{kj} = \int_{\Omega} \sigma \nabla \phi_k \cdot \nabla \phi_j dx + \sum_{l=1}^L \frac{1}{z_l} \int_{e_l} \phi_k \phi_j dS. \quad (2.62)$$

That is

$$B_{kj} = \sum_{i \in \text{supp}(k,j)} A_i \sum_{l=1}^2 \sum_{m=1}^2 \frac{\partial \phi_k^{(i)}}{\partial x_l} \bar{\sigma}_{lm}^{(i)} \frac{\partial \phi_j^{(i)}}{\partial x_m} + \sum_{l=1}^L \frac{1}{z_l} \int_{e_l} \phi_k \phi_j dS. \quad (2.63)$$

where $\text{supp}(i, j)$ is the support of the edge (i, j) , $\bar{\sigma}_{lm}^{(i)}$ is the average of the nodal values σ_{lm} of the k th element and A_i is the area of the i th element in the mesh.

- ii. The entries of the block matrix C are determined as follows: For $1 \leq \mathbf{k} \leq \mathbf{N}, \mathbf{N} + 1 \leq \mathbf{j} \leq \mathbf{N} + (\mathbf{L} - 1)$. In this case $u^h \neq 0, U^h = 0, v = 0$, and $V \neq 0$. The sesquilinear form simplifies to

$$B_s((u^h, 0), (0, V)) := - \sum_{l=1}^L \frac{1}{z_l} \int_{e_l} u^h V_l ds = I_1 - I_{j+1} \quad (2.64)$$

Therefore, entries of the matrix C become,

$$C_{kj} = - \left[\frac{1}{z_l} \int_{e_l} \phi_k(\vec{n}_j)_l ds \right] \quad (2.65)$$

$$= - \left[\frac{1}{z_l} \int_{e_l} \phi_k ds - \frac{1}{z_j + 1} \int_{e_l} \phi_k ds \right] \quad (2.66)$$

iii. The entries of the block matrix \tilde{C} are determined as follows:

For $\mathbf{N} \leq \mathbf{k} \leq \mathbf{N} + (\mathbf{L} - 1)$, $\mathbf{1} \leq \mathbf{j} \leq \mathbf{N}$. Here $u^h = 0, U^h \neq 0, v \neq 0, V = 0$. Thus $B_s((u^h, U^h), (v, 0))$ is given by

$$B_s((0, U^h), (v, 0)) = - \sum_{l=1}^L \frac{1}{z_l} \int_{e_l} U^h v_l ds = 0$$

Thus the kj th entry of the matrix \tilde{C} is

$$\tilde{C} = - \left[\frac{1}{z_l} \int_{e_l} \phi_j ds - \frac{1}{z_l + 1} \int_{e_{j+1}} \phi_{j+1} ds \right] \quad (2.67)$$

iv. The entries of the block matrix D are determined as follows:

For $\mathbf{N} \leq \mathbf{k}, \mathbf{j} \leq \mathbf{N} + (\mathbf{L} - 1)$. Here $u^h = 0, U^h \neq 0, v = 0, V \neq 0$ The sequilinear form is given by

$$B_s((0, U^h), (0, V)) := \sum_{l=1}^L \frac{1}{z_l} \int_{e_l} U^h V_l ds = I_1 - I_{j+1} \quad (2.68)$$

This the entries of matrix D are given by

$$D_{kj} = \begin{cases} \frac{|e_1|}{z_1} + \frac{|e_{j+1}|}{z_{j+1}}, & j = k - N \\ \frac{|e_1|}{z_1}, & j \neq k - N \end{cases} \quad (2.69)$$

Solving (2.56) gives us the coefficients $\beta_{(k-N)}$ required for the voltages U^h on the electrodes.

Shown below are the potentials obtained by implementing the forward code in MATLAB. The complete electrode model with 32 electrodes is considered for the forward model. We consider a simple test case here. The adjacent current pattern, that is skip 0 current pattern is applied with a current of magnitude $1A$, which is higher than a physically realistic model. Circular geometry with a circular inclusion is assumed. The contact impedance is assumed to be 2.4 mili-ohms per meter. The electrode placement on the surface of the body is shown below.

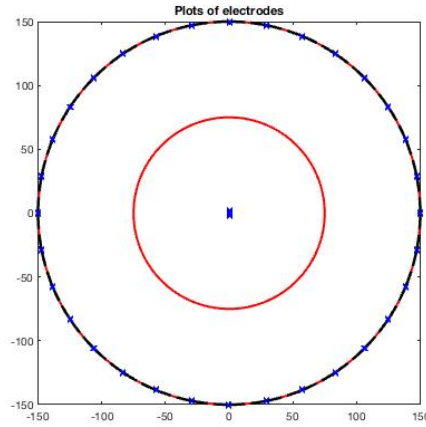


Figure 2.1: The placement of electrodes on the exterior of a circular domain with a circular inclusion shown in red. Here the first electrode is placed on the horizontal axis at 0 degrees and the electrodes are counted counter clockwise. The conductivity is given by σ_{int}^{ver} inside the circular inclusion and σ_1 in the annulus outside the circular inclusion.

The potential on the electrodes where in the interior the preference for the direction of current is vertical as opposed to horizontal and with the reversal of the preference for the direction of current is given below. The background conductivity in both cases is assumed to be isotropic, given by $\sigma_1 = \begin{pmatrix} 1 & 0 \\ 0 & 1 \end{pmatrix}$ and that inside the circle where vertical direction for the flow of current preferred

over the horizontal, given by $\sigma_{int}^{ver} = \begin{pmatrix} 1 & 0 \\ 0 & 4 \end{pmatrix}$ and that of the horizontal direction preference over that of vertical, given by $\sigma_{int}^{hor} = \begin{pmatrix} 4 & 0 \\ 0 & 1 \end{pmatrix}$ are shown below.

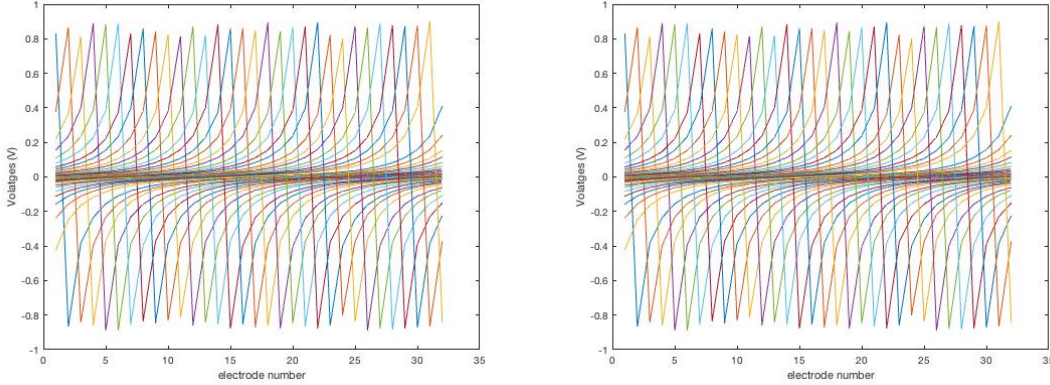


Figure 2.2: Left: The potential on the 32 electrodes due to 31 linearly independent current patterns applied to the electrodes when the conductivity in the circular inclusion is assumed to be σ_{int}^{ver} . Right: The potential on the 32 electrodes due to 31 linearly independent current patterns applied to the electrodes when the conductivity in the circular inclusion is assumed to be σ_{int}^{hor} . Each color represents a volatge arising from a different current pattern.

2.7 Inverse problem

The aim is to compute an approximation for the conductivity distribution inside the body based on the measured voltages and injected currents. We assume that the conductivity can be diagonalized for every point in the domain. This is consistent with the assumption of our problem that σ is a symmetric positive definite matrix in \mathbb{R}^n . Diagonalization is defined using the eigenvalue decomposition by an orthonormal transformation as $\sigma = \mathbf{A}\mathbf{D}\mathbf{A}^T$ where $\mathbf{A} = [\mathbf{a}_1, \mathbf{a}_2]$ is a known matrix of orthonormal eigenvectors \mathbf{a}_i and $\mathbf{D} = \text{diag}(d_1, d_2)$ is a matrix of real positive eigenvalues. The nonlinear forward problem can be represented as $\mathbf{V} = \mathbf{F}(\mathbf{D}) + \epsilon$, where $F(D) : \mathbb{R}^{N \times 2} \rightarrow \mathbb{R}^M$ is the forward nonlinear operator, $\mathbf{V} \in \mathbb{R}^M$ is the measured data, that is voltages on the electrodes

due to different current patterns and $\mathbf{D} \in \mathbb{R}^{N \times 2}$ is the unknown conductivity to be determined. The noise in the measured data is considered to be $\epsilon \sim \mathcal{N}(\mathbf{0}, \gamma^2 \mathbf{I}_m)$

Abascal et al [1] did a numerical study on the feasibility of the recovery of a piecewise linear finite element conductivity tensor in anisotropic media with known eigenvectors representing the directions of anisotropy from complete boundary data. The minimization of the least squares functional

$$\mathcal{L}(\mathbf{D}) = \frac{1}{2} \|\mathbf{F}(\mathbf{D}) - \mathbf{V}\|_2^2 \quad (2.70)$$

was done using gradient-based approach to recover the eigenvalues \mathbf{D}

In this thesis, we formulate the priors for the unknown conductivity \mathbf{D} using our information on the preferential direction for the flow of current. Additionally, we derive the probability distribution for the unknown conductivity using these priors and show that this results in generalized Tikhonov regularization.

2.7.1 Construction of Priors

Let $A : \Omega \rightarrow \mathbb{R}^{2 \times 2}$ denote a matrix-valued mapping on Ω . For each $x \in \Omega$, let $A(x)$ be a positive semidefinite and symmetric matrix. Let the eigenvalue decomposition of A be given by $A = V \Delta V^T$ where $V = V(x)$ is an orthonormal matrix and $\Delta = \Delta(x) = \text{diag}(\delta_1(x), \delta_2(x))$, where $\delta_1 \geq 0$ and $\delta_2 \geq 0$.

Consider the functionals $W_1(d_1)$ and $W_2(d_2)$ to be given by

$$W_1(d_1) = \int_{\Omega} \|A(x) \nabla(d_1(x))\|_{\mathbb{R}^N}^2 dx \quad (2.71)$$

and

$$W_2(d_2) = \int_{\Omega} \|A(x) \nabla(d_2(x))\|_{\mathbb{R}^N}^2 dx \quad (2.72)$$

By the eigenvalue decomposition, we have ,

$$A(x) \nabla d_1(x) = \sum_{j=1}^2 (\delta_j(x) v_j^T(x) \nabla d_1(x)) v_j(x) \quad (2.73)$$

and

$$A(x)\nabla d_2(x) = \sum_{j=1}^2 (\delta_j(x)v_j^T(x)\nabla d_2(x))v_j(x) \quad (2.74)$$

Thus, by the orthonormality of $V(x)$, we have

$$W_1(d_1) = \sum_{j=1}^2 \int_{\Omega} |\delta_j(x)v_j^T(x)\nabla(d_1)|_{\mathbb{R}^N}^2 dx \quad (2.75)$$

and

$$W_2(d_2) = \sum_{j=1}^2 \int_{\Omega} |\delta_j(x)v_j^T(x)\nabla(d_2)|_{\mathbb{R}^N}^2 dx \quad (2.76)$$

Therefore, $W(d_i)$ measures the square integral norm of the derivative of d_i in the directions v_j with weights δ_j . These functions $W(d_i)$, therefore, can be used in building prior probability density of d_i and d_2 .

Let us assume that the conductivity that we are interested in recovering has a preference of vertical direction, that is y-direction over horizontal, that is x-direction. Let us further assume that the probability density for the diagonal conductivities are of the form

$$p_{prior}(d_1) = \exp(\beta^2 W_1(d_1)) \quad (2.77)$$

and

$$p_{prior}(d_2) = \exp(\beta^2 W_2(d_2)) \quad (2.78)$$

From Bayes' law, we have

$$p(V|d_1) \propto p(d_1|V)p(d_1) \quad (2.79)$$

and

$$p(V|d_2) \propto p(d_2|V)p(d_2) \quad (2.80)$$

Then, the maximum a posterior density for d_1 and d_2 is found by minimizing

$$\|\mathbf{F}(\mathbf{D}) - \mathbf{V}\|^2 + \beta^2 W_1(d_1) \quad (2.81)$$

and

$$\|\mathbf{F}(\mathbf{D}) - \mathbf{V}\|^2 + \beta^2 W_2(d_2) \quad (2.82)$$

2.7.2 Numerical implementation

Thus, searching for maximum a posterior (MAP) estimator for d_1 and d_2 can be seen as solving an inverse problem using Tikhonov regularization. For a piecewise linear conductivity of the form $\sigma = \sum_{j=1}^N \sigma_j \varphi_j$, the gradient of conductivity $\nabla \sigma$ is a piecewise constant function. In order to find the MAP estimator, we need to construct the matrix mapping A such that it incorporates the preference of conductivity in the y-direction over the x-direction. This can be done by choosing the standard orthogonal vectors for the Euclidean space as the choice of orthogonal vectors v_k , that is $v_1 = (1, 0)^T$ and $v_2 = (0, 1)^T$. Then, for each element Ω_j , the matrix $A(x)$ will be defined by

$$A(x)|_{\partial\Omega_j} = \delta_1^j v_1^j (v_1^j)^T + \delta_2^j v_2^j (v_2^j)^T \quad (2.83)$$

To account for the preference of conductivity in y-direction, we make the weight for x-direction much smaller compared to the weight in y-direction. That is, we let $\delta_1 < 1$, and $\delta_2 = 1$. We then solve the (2.81) and (2.82) using Gauss-newton method, which is outlined below

$$\mathbf{d}_i^{k+1} = \mathbf{d}_i^k + \Delta \mathbf{d}_i^k \quad (2.84)$$

where

$$\mathbf{d}_i^k = -H^{-1} \nabla \Phi \quad (2.85)$$

$$\Phi = (\|\mathbf{V} - \mathbf{F}(\mathbf{D})\|)^2 + \|\beta^2 W_i\|^2 \quad (2.86)$$

and H is the Gauss-Newton approximation to the Hessian matrix of Φ . The Hessian is given by

$$H = -(J^T J + \alpha L^T L)^{-1} [J^{-1} (V - F(D)) - \alpha L^T L(D)] \quad (2.87)$$

2.7.3 Computation of the Jacobian

The computation of the Jacobian J from the forward map $\mathbf{F}(\mathbf{D})$ is as follows: Let $d_{\delta\sigma}F_{ij}$ be the directional derivative of the forward operator F_{ij} in the direction of $\delta\sigma$

$$d_{\delta\sigma}F_{ij} = \nabla_{\sigma}F_{ij} \cdot \delta\sigma \quad (2.88)$$

Here i represents the various current injection patterns and j represents the voltage on the j th electrode, due to i th current pattern.

The directional derivative is given by

$$d_{\delta\sigma}F_{ij} = - \int_{\Omega} d\mathbf{r} (\nabla u_i) \cdot (\delta\sigma \nabla u_j^*) = - \int_{\Omega} \sum_{l,m=1}^2 \frac{\partial u_i}{\partial x_m} \delta\sigma_{lm} \frac{\partial u_j^*}{\partial x_m} \quad (2.89)$$

The directional derivative is the product of current and measurement, where u is the forward solution and u^* is the adjoint forward solution which is obtained by considering the measurement points as the injection points. The Jacobian with respect to the conductivity coefficients σ_{lm}^s at the node s is obtained by the substitution of the basis in (2.89) and given by

$$J = - \int_{\Omega} d\mathbf{r} \phi_s(r) \left(\frac{\partial u_i}{\partial x_m} \frac{\partial u_j^*}{\partial x_m} + (1 - \delta_{lm}) \frac{\partial u_i}{\partial x_m} \frac{\partial u_j^*}{\partial x_m} \right) \quad (2.90)$$

$$= - \sum_{k \in \text{supp}(\phi_s)} \frac{A_k}{3} \frac{\partial u_i}{\partial x_m} \frac{\partial u_j^*}{\partial x_m} \quad (2.91)$$

2.7.4 Implementation of the reconstruction algorithm

Implementation of the reconstruction algorithm: In the simulation the conductivity was assumed to prefer y-direction over the x-direction. The conductivity distribution was assumed to be

$\sigma = \begin{pmatrix} 1 & 0 \\ 0 & 4 \end{pmatrix}$ in the interior of the circle used for the forward problem. The voltages on the

electrodes were simulated using a 32 electrode placement over the boundary of the domain with 31 current injection patterns.

The reconstructions were done on a coarser mesh with 4217 elements and 3161 nodes. Assuming the weight on diagonal conductivity d_1 as $\delta = 0.1$ and on d_2 as $\delta_2 = 1$, the reconstructions were performed. The reconstructions of the diagonal conductivity are as shown below in Figure 2.3. It can be seen from Figure 2.3 that the interior conductivity in the y-direction is higher than the x-direction.

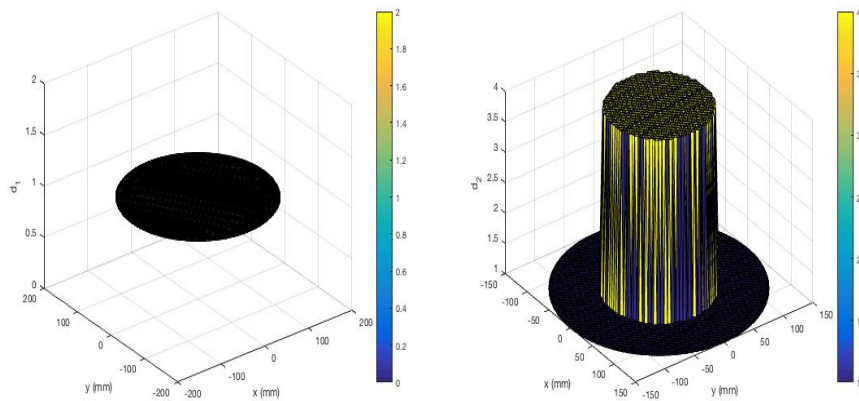


Figure 2.3: Left: Reconstruction of the diagonal conductivity along the x-axis d_1 . Right: Reconstruction of the diagonal conductivity along the y-axis d_2 . It is clear that d_1 is less than that of d_2 values.

2.8 Conclusions and Future work

1. The computational Bayesian framework that allows for the priors to incorporate the directional preference of the conductivity is derived. If the conductivity is assumed to be diagonalizable, the reconstructions for the diagonal conductivity is shown possible with the maximum a posterior estimates.

Future work in this direction is to do an Uncertainty Quantification analysis, which will require sampling using, for example Gibbs sampling or Randomize-then-Optimize process [15].

2. The linearized injectivity of the anisotropic EIT problem can be further developed into a direct reconstruction algorithm. We can formulate the bilinear form which in turn gives us the inverse Fourier transform for the isotropic problem. This results in a direct reconstruction algorithm, which can be implemented on both synthetic data and real data.

Chapter 3

Impact of structural changes in the reconstruction using 2-D D-bar algorithm

3.1 Introduction

In thoracic imaging, which is a current research focus of the EIT lab in the Department of Mathematics at Colorado State University, one promising application is to monitor pulmonary ventilation and fluid volume changes. Diseases that cause variation in the lung composition can be monitored by EIT by measuring the lung resistivity changes. Since the lung is the largest organ in the thorax, the resistivity change can be more accurately measured by EIT. Pulmonary applications of EIT require a good understanding of what contributes to the measured resistivity changes. It is often assumed that the measured resistivity change in EIT is caused by actual resistivity change of a tissue or in some cases the volume change of the vessel. Structural changes such as location of organs or vessels, or the overall cross-sectional area are rarely considered. Respiratory activity involves a rhythmic movement of the rib cage by as much as 10% of the anterior-posterior dimension. This results in a movement of the electrodes which violates the assumption of constant geometry. This tends to introduce artifacts into the reconstructed images which needs to be accounted for in image interpretation [120].

3.2 Literature Review

3.2.1 Effect of domain shape on reconstruction

Jain et al, in 1997, studied the EIT problem with complex conductivity distributions with non-circular boundary [6]. They showed that for a homogenous conductivity in an elliptical body with the axis ratio of 0.73 had an artifact at the center with an error of 20% when image was constructed assuming the boundary to be circular. The error increased to 37% when the axis ratio was 0.64. A

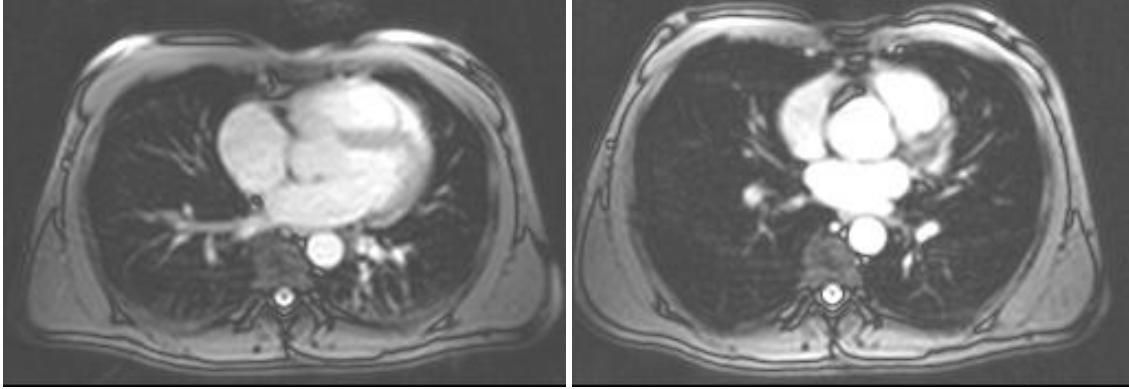


Figure 3.1: Change in the overall cross-sectional area during inhalation and exhalation. (Source: [120])

reconstruction algorithm with the same axis ratio as the elliptical boundary reduced the error in the conductivity values within 0.5% of the actual values. In the year 2005, Kolehmainen et al showed that an inaccurate model for the boundary causes errors in the reconstruction [90]. The authors introduced a new algorithm to find deformed image of the original isotropic conductivity based on the theory of Teichmüller spaces. In 2007, Murphy et al computed the scattering transform on an ellipse to get static conductivity reconstructions of conductive and insulative targets in a saline tank using D-bar method [6]. They showed that the spatial artifacts in the images significantly reduced when the domain was modeled properly. In the year 2009, Murphy and Mueller computed the scattering transform for the D-bar method on chest-shaped domain [48]. In this paper the chest shape was approximated by a parametrization of the boundary by a function $r(\theta)$, with the arc length as $d\sigma = \sqrt{r^2 + (r')^2}d\theta$. With this parametrization it was shown that the reconstructions were improved from circular approximation of the boundary. All of these results illustrates that using proper shape of the domain increases the robustness of the reconstructions. The next question in this direction would be the effect of changes in the size of the boundary, since it is clear that respiratory activity involves a movement of the rib cage.

3.2.2 Effect of dynamic changes in the boundary on reconstruction

Zhang et al [120] studied the influence of chest expansion during respiration on EIT images using a two dimensional thorax finite element model. In this paper the effect of electrode movement

due to chest expansion is modeled. The movement of any point (x, y) at a cross-section of the 3D throax model was described by the following:

$$\bar{d} = M \left[(y - y_c)\bar{y} + L \frac{APD}{LD} (x - x_c)\bar{x} \right] \quad (3.1)$$

where (x_c, y_c) are coordinates of the center of the thorax, \bar{d} is the displacement, \bar{x}, \bar{y} unit vectors in lateral and anterior-posterior (AP) directions. APD is the displacement in the AP direction and LD is the displacement in the lateral dimesion. The parameter L represents the ratio of the lateral to AP displacement and M represents fractional expansion in the AP direction. The results showed that thorax expansion contributed to the measured change in conductivity and accounted for up to 20% of the reconstructed image amplitude in the broad zone at the center of the image [?]. Zhang et al showed that with the increase of simulated chest expansion, the percentage contribution of chest expansion relative to lung resistivity change in the EIT image remained relatively constant [?]

Of interest to the EIT Lab at CSU is the imaging of lung function in human subjects. One of the important applications of EIT is pulmonary imaging. To diagnose and assess obstructive and restrictive lung disease, physicians use Pulmonary Function Test (PFT) tests. In a PFT, a person breathes in to mouthpiece that is connected into an instrument called a spirometer. The spirometer records the amount and the rate of air that is breathed in and out over a specified time. Often this requires forced exhalation after a deep breath. Flow Volume loops that are plots of volume vs flow rate, parametrized by time are computed during PFTs. The Figure 3.2 below shows EIT data collected during spirometry.



Figure 3.2: The EIT data collected during a spirometry test.

It is clear that the size of the domain increases significantly during the deep inhalation and exhalation, required for PFTs. Thus we intend to study the effect of the change in domain size on the reconstructions. The current D-bar direct reconstruction algorithm that we are using on the data from Children’s Hospital Colorado, Aurora, Colorado, assumes the boundary to be static during reconstructions. However, during the Pulmonary Function Tests, we have consistently observed that the exterior (chest) changes considerably during the big breath in and exhale part of it. Therefore, we would like to implement a dynamically changing boundary boundary to our current D-bar reconstruction algorithm to better the spatial resolution.

3.3 Implementation of dynamic changes in boundary

To implement a dynamically changing boundary in the D-bar, we will use time traces of the data to inform the D-bar algorithm about the stage in the ventilatory cycle, so that the boundary changes do not have to rely on videos or additional information. The D-bar Algorithm discussed in Chapter 1 is repeated here for convenience.

Step 1: Consider the input of noisy EIT data Λ_σ and the noise amplitude $\delta > 0$

Step 2. Solve the boundary integral equation

$$\Psi(z, k)|_{\partial\Omega} = e^{ikz}|_{\partial\Omega} - \int_{\partial\Omega} G_k(z - \zeta)(\Lambda_\sigma - \Lambda_1)(\Psi(\zeta, k))ds(\zeta)$$

to get $\Psi|_{\partial\Omega}$.

Step 3. Using $\Psi|_{\partial\Omega}$ compute the scattering transform $\mathbf{t}(k)$ by

$$\mathbf{t}(k) = \int_{\partial\Omega} e^{i\bar{k}z}(\Lambda_\sigma - \Lambda_1)\Psi(z, k)ds(z)$$

Step 4. Use the scattering transform $\mathbf{t}(k)$ to solve the Fredholm integral equation

$$\mu(z, k) = 1 + \frac{1}{4\pi^2} \int_{\mathbb{R}^2} \frac{\mathbf{t}(k')}{(k - k')k'} e^{-i(k'z + \bar{k}'z)} \overline{\mu(z, k')} dk' \quad (3.2)$$

for $\mu(z, k)$

Step 5: From $\mu(z, k)$ compute $\sigma(z)$ using $\mu(z, 0) = \sqrt{(\sigma(z))}$

To implement a dynamically changing boundary in the D-bar algorithm, we use a principle component analysis (PCA) of a preliminary reconstruction to inform the D-bar algorithm about the stage in the ventilatory cycle, so that boundary changes do not have to rely on videos or additional information. A PCA of the voltage data would serve equally well. An example of PCA is shown in Figure 3.3

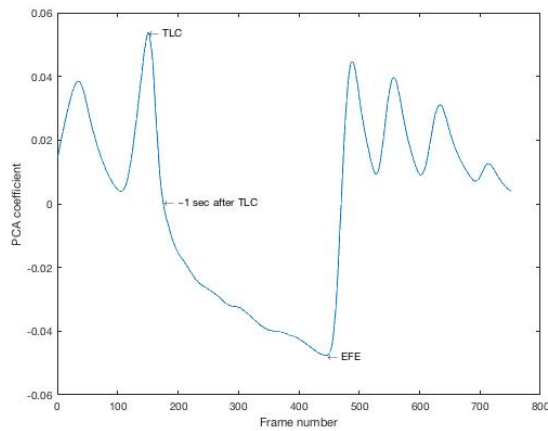


Figure 3.3: PCA output during a spirometry test used for identifying the key time points for the implementation of the dynamically changing boundary. TLC on the plot corresponds to the maximum inhalation and EFE corresponds to maximum exhalation.

The percentage of change in the outer boundary between a normal exhale and maximal inhale was taken to be 12.5% and between a maximum inhale and maximum exhale was found to be 4% of the boundary measured. This was estimated by repeatedly measuring on a healthy subject during maximum inhale and exhale. The boundary corresponding to the first frame was data was estimated by a flexible ruler. These data points was then scaled to a maximum radius of 1 and then used to construct a Fourier series approximation to the boundary function $r(\theta)$

$$r(\theta) = a_0 + \sum_{i=1}^N a_i \cos(\theta) + b_i \sin(\theta),$$

where the coefficients are chosen so as to minimize the error $\|r(\theta_{meas}) - r_{meas}\|$ over all the measurements in a least squares sense. Once both boundary functions are defined, given a discrete set of angles $\theta_i, 0 = \theta_1, \dots, \theta_M = 2\pi - \Delta\theta_M$ the boundary function $r(\theta)$ for frames between maximal inhalation and exhalation is interpolated for each $\theta_i, i = 1, \dots, M$. To do the interpolation, the number of frames N between a given maximal inhalation and exhalation was calculated from the PCA, and the radius $r(\theta_i)$ of the boundary was interpolated between the radius corresponding to maximum inhale $r_{max}(\theta_i)$ and the radius corresponding to maximum exhale $r_{min}(\theta_i)$ according to the formula

$$r_j(\theta_i) = r_{min}(\theta_i) + j(r_{max}(\theta_i) - r_{min}(\theta_i))/N,$$

where j denotes the number of frames since the most recent maximal exhalation..The organ boundaries can be treated in the same manner.

Due to equation $R_\sigma(m, n) = (s_\ell J^m, \mathbf{v}^n)_L$, the discretized DN map, $\Lambda_\sigma : u|_{\partial\Omega} \rightarrow \sigma \frac{\partial u}{\partial \nu}|_{\partial\Omega}$ changes at each frame of the respiratory process. The Boundary integral for $\Psi(z, k)$ in step 2 of the algorithm, which depends on the difference in the DN maps $\Lambda_\sigma - \Lambda_1$ and is integrated over the boundary $\partial\Omega$, changes. This leads to changes in the scattering transform $\mathbf{t}(k)$ that is dependent on difference in DN maps $\Lambda_\sigma - \Lambda_1$, boundary $\partial\Omega$, and the boundary integral $\Psi(z, k)$, in turn changing in the interior conductivity σ . We expect that the images that are obtained by taking into account these changes will reduce the artifacts.

3.4 Results

In this section, the reconstructions of the human data where the movement of the boundary was taken into account is presented. The data were collected at the Children's Hospital Colorado, Aurora, CO under the approval of the Colorado Multiple Institutional Review Board (COMIRB) (approval number COMIRB 14-0652). The EIT data was collected on 25 electrodes of width 2.22 cm and height 3.33 cm for one specific subject studied here. Principle Component Analysis (PCA) of the data was used to identify the frames corresponding to maximum inhalation and maximal exhalation. The perimeter of the boundary for this subject was found to be 0.7112 m.

The reconstructions of the human data collected during a spirometry test that accounts for the dynamically changing boundary are plotted in Figure 3.4 and Figure 3.5. Here, the blue color on the color bar represent low conductivity and red color on the color bar represent the higher conductivity.

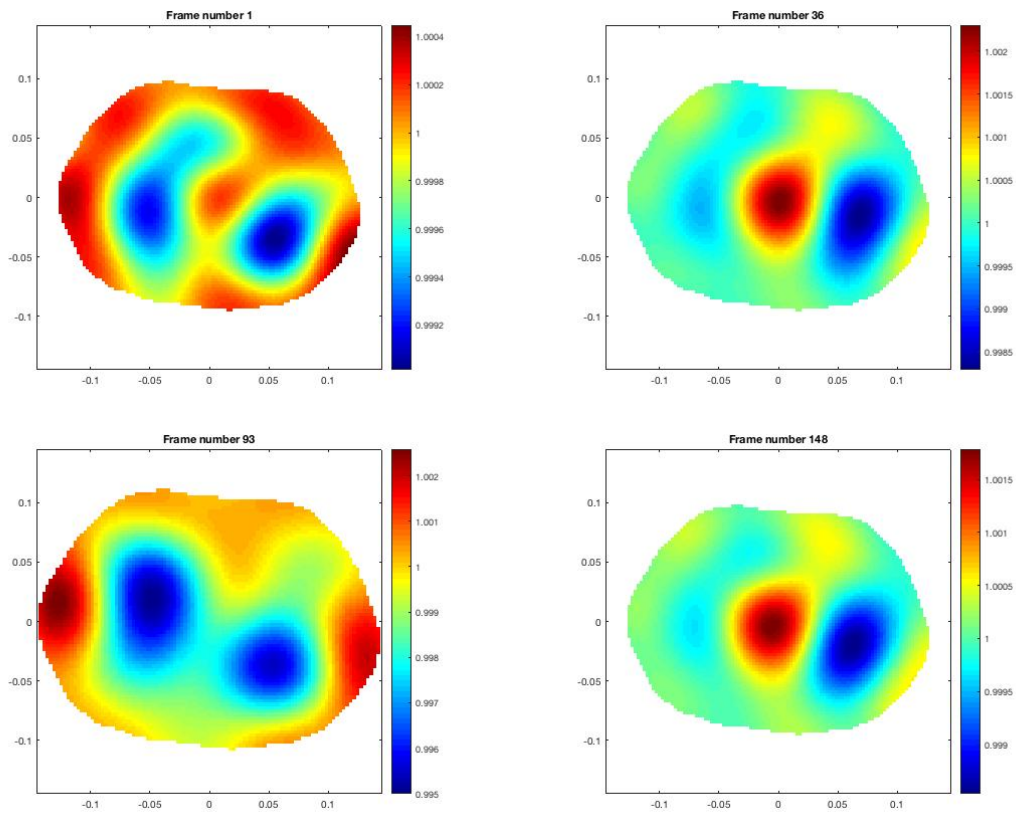


Figure 3.4: Plots of reconstructions of the conductivity that corresponding to first frame, the first exhalation, first inhalation, consequent exhalation, maximum inhalation and maximum exhalation and the consecutive breaths

The reconstructions of the human data that accounts for the dynamically changing boundary and that do not account for the dynamically changing boundary are given side by side for the frames that correspond to the first exhalation, first inhalation, consequent exhalation, maximum inhalation and maximum exhalation and the consecutive breaths after that are shown in Figure 3.6 and Figure 3.7

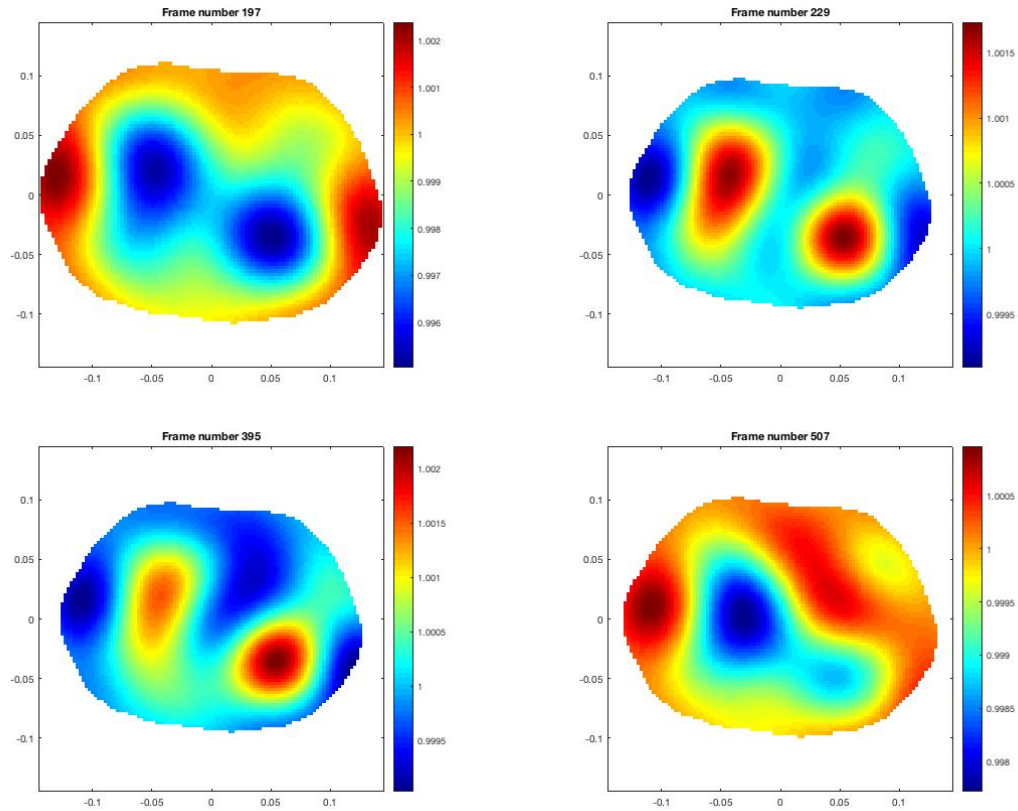


Figure 3.5: Plots of reconstructions of the conductivity that corresponding to first frame, the first exhalation, first inhalation, consequent exhalation, maximum inhalation and maximum exhalation and the consecutive breaths

3.5 Discussions

The change in the conductivity value when computed with and without dynamically changing boundary for each of the pixels for frames 36, 93 and 148 are plotted in Figure 3.8.

For the frame 36, it is clear from the difference in conductivity plot that the artifacts to the left are reduced where as the shape of the left lung gets better with dynamically changing boundary.

For the frame 93, it is clear that from the the artifacts to the left are reduced while the shape of the lungs gets better with the incorporation of dynamically changing boundary.

For the frames 148 and 229, the frames corresponding to maximum inhalation and maximum exhalation, there is not much difference in the conductivity values with the incorporation of the dynamically changing boundary. This is to be expected since, maximum inhalation boundary are the same for dynamically changing and regular D-bar algorithms. For the minimum exhalation,

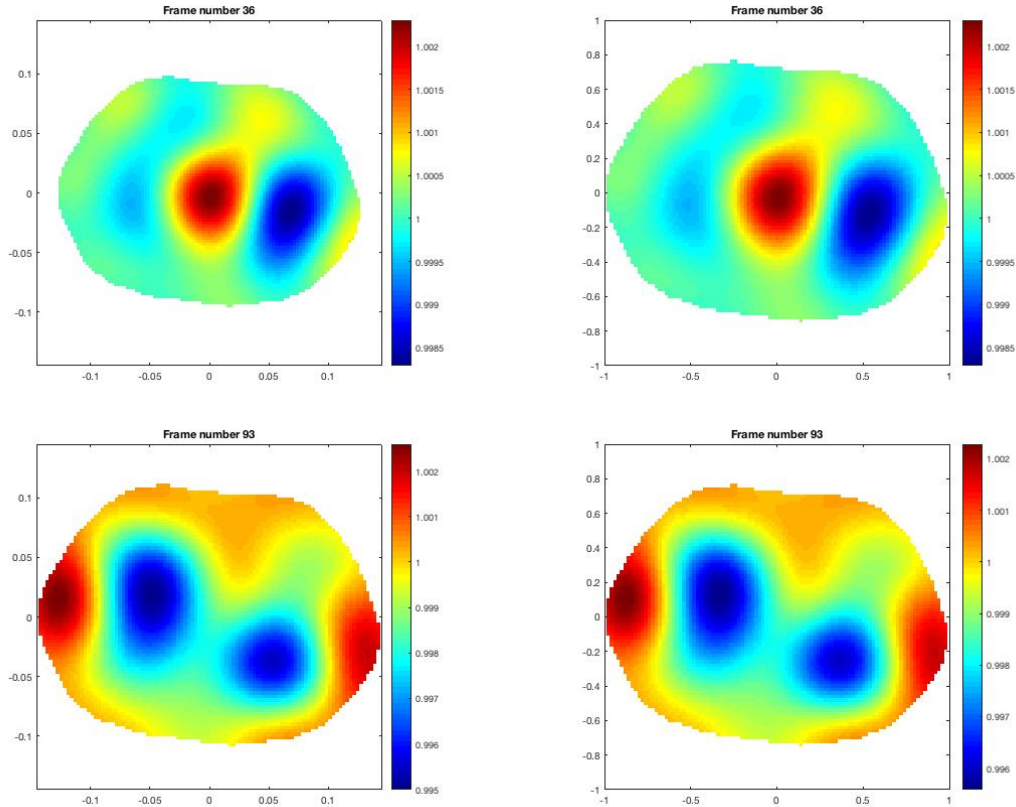


Figure 3.6: The reconstructions of the EIT data for the same subject with and without accounting for dynamically changing boundary.

since the conductivity values are the difference from this particular frame, we do not expect significant difference in the reconstructions made by accounting for the dynamically changing values as against the reconstructions made by regular D-bar method.

3.6 Conclusions

The dynamically changing boundary was implemented in [9]. In this paper we implemented dynamic boundaries to compute spatial priors in the 2-D D-bar algorithm and the effectiveness of the method was demonstrated on human subject ventilatory data.

As a part of this thesis, I have actively participated in data collection and image reconstruction with D-bar and data analysis on cystic fibrosis patients at Children’s Hospital Colorado. This resulted in publication of two papers of which I am a co-author.

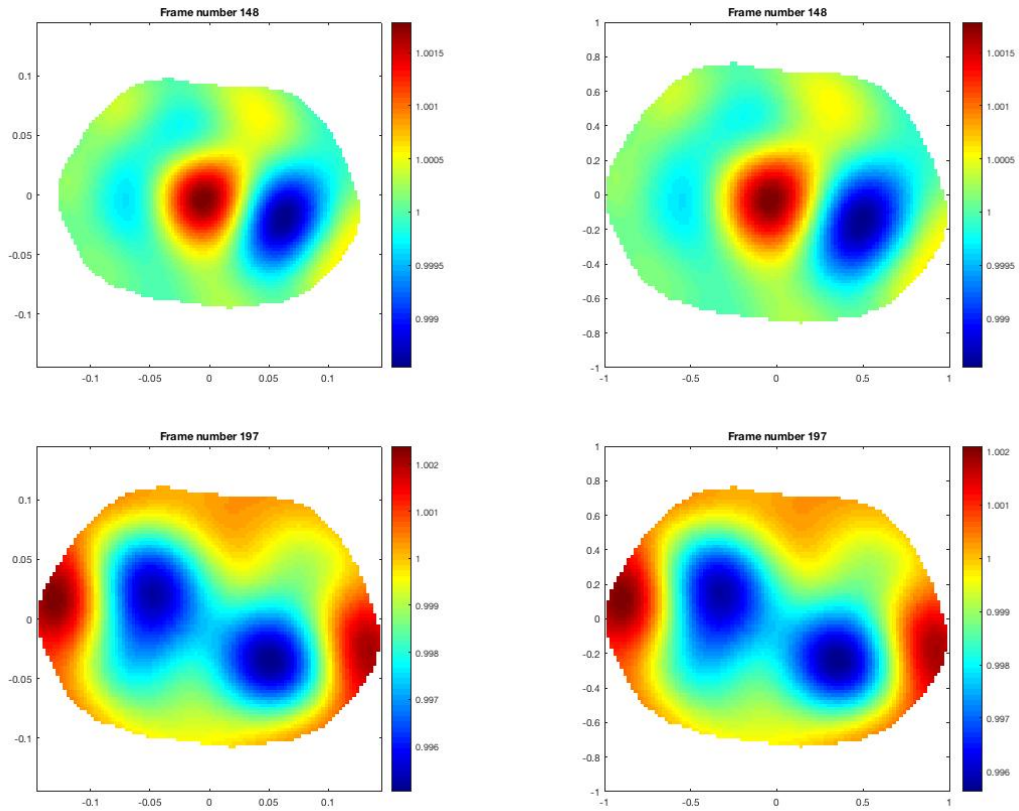


Figure 3.7: The reconstructions of the EIT data for the same subject with and without accounting for dynamically changing boundary.

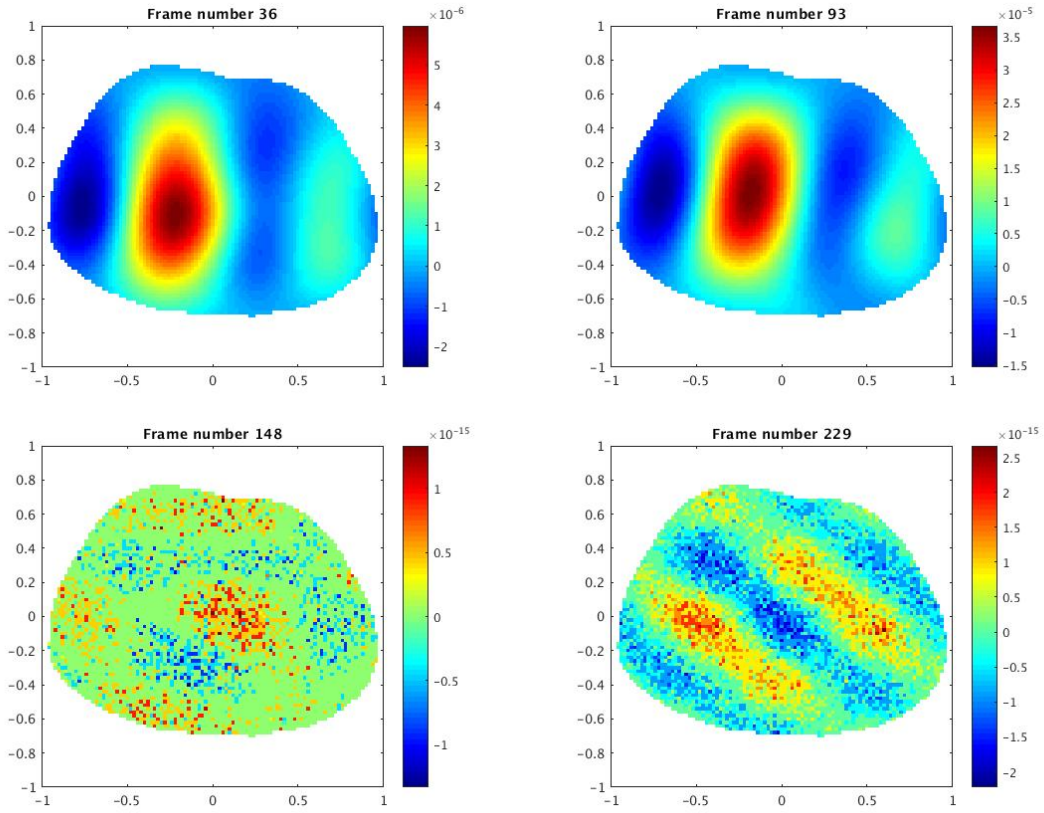


Figure 3.8: Difference in the conductivity computed with and without the dynamically changing boundary values for frames 36,93,148,229

Bibliography

- [1] J-F. P. J. Abascal, W. R. B. Lionheart, S. R. Arridge, M. Schweiger, D. Atkinson D. S. Holder. Electrical Impedance tomography in anisotropic media with known eigen vectors. *Inverse Problems*, 27(6):258–268,2011.
- [2] J-F. P. J. Abascal, S. R. Arridge, D. Atkinson, R. Horesh, L. Fabrizi, M. De Lucia, L. Horesh, R. H. Bayford, D. S. Holder. Use of anisotropic modelling in electrical impedance tomography; description of method and preliminary assessment of utility in imaging brain function in the adult human head. *Neuroimage*, 43(2):258–268,2008.
- [3] A. Adler, B. Grychtol, R. Bayford. Why is EIT so hard, and what are we doing about it. *Physiological measurement*, 36(6):1067, 2015.
- [4] M. Akthaari, M. Mandelkern, D. Bui, N. Salamon, H. V. Vinters, G. W. Mathern Variable Anisotropic Brain Electrical Conductivities in Epileptogenic Foci. *Brain Topography*, 23(3):292–300, 2010.
- [5] G. Alessandrini. Stable determination of conductivity by boundary measurements. *Applicable Analysis*, 27(1–3):153–172,1988.
- [6] G. Alessandrini. Singular solutions of elliptic equations and the determination of conductivity by boundary measurements. *Journal of Differential Equations*, 84(2):252–272,1990.
- [7] A. Allers, F. Santosa. Stability and resolution analysis of a linearized problem in electrical impedance tomography. *Inverse Problems*, 7(4):515–533,1991.
- [8] G. Alessandrini, R. Gaburro. Determining Conductivity with special anisotropy by boundary measurements. *SIAM J. MATH. ANAL*, 33(1):153–171, 2001.
- [9] M. Alsaker, J. L. Mueller, R. Murthy. Dynamic optimized priors for D-bar reconstructions of human ventilation using electrical impedance tomography *Journal of Computational and Applied Mathematics* In review.

- [10] K. Astala, J. L. Mueller, L. Päivärinta, A. Perämäki, S. Siltanen. Direct electrical impedance tomography for nonsmooth conductivities. *Inverse Problems and Imaging*,5(3)531–549, 2011.
- [11] K. Astala, M. Lassas, L. Päivärinta. Calderón’s Inverse Problem for the Anisotropic Conductivity in the plane. *Communications in Partial Differential Equations*,30(1–2) , 2005.
- [12] A. P. Bagshaw, A. D. Liston, R. H. Bayford, A. Tizzard, A. P. Gibson, A. T. Tidswell, M. K. Sparkes, H. Dehghani, C. D. Binnie, D. S. Holder Electrical impedance tomography of human brain function using reconstruction algorithms based on finite element method *NeuroImage*, 20(2): 752–764, 2003.
- [13] D. C. Barber, B. H. Brown. Applied potential tomography *Journal of physics. E. Scientific instruments*, 17(9):723–733, 1984.
- [14] D. C. Barber, B. H. Brown. Progress in electrical impedance tomography *Inverse problems in partial differential equations*, 151–164, 1990.
- [15] J. M. Bardsley, A. Seppänen, A. Solonen, H. Haario, J. Kaipio Randomize-Then-Optimize for Sampling and Uncertainty Quantification in Electrical Impedance Tomography *SIAM J. Uncertainty Quantification*, 3,1136–1158, 2015.
- [16] R. Barrett, M. Berry, T. F. Chan, J. Demmel, J. Donato, J. Dongarra, V. Eijkhout, R. Pozo, C. Romine, H. Van der Vorst. *Templates for the Solution of Linear Systems: Building Blocks for Iterative Methods, 2nd Edition*,SIAM, Philadelphia, PA, 1994.
- [17] U. Baysal, B. M. Eyüboğlu use of a priori information in estimating tissue resistivities - a simulation study. *Physics in Medicine and Biology*, 43(12):3589–3606, 1998.
- [18] R. Beals, R. Coifman Scattering, transformations spectrales et équations d’évolution non linéaire ii. *Séminaire Équations aux dérivées partielles (Polytechnique)*, 1–8, 1982.

- [19] R. Beals, R. R. Coifman. Multidimensional inverse scattering and nonlinear partial differential equations. In *Proc. Symp. Pure Math*, volume 43, 45–70, 1985.
- [20] C. A. Berenstein, E. C. Tarabusi. Inversion formulas for the k -dimensional radon transform in real hyperbolic spaces. *Duke Mathematical Journal*, 62(3):613–631, 1991.
- [21] J. Bikowski, J. L. Mueller. 2D EIT reconstructions using Calderóns method. *Inverse Problems and Imaging*, 2(1):43–61, 2008.
- [22] A. Binley, S. Henry-Poulter, B. Shaw. Examination of solute transport in an undisturbed soil column using electrical resistance tomography. *Water Resources Research*, 32(4):763–769, 1996.
- [23] R. S. Blue, D. Isaacson, J. C. Newell Real-time three-dimensional electrical impedance imaging. *Physiological Measurement*, 21(1):15–26, 2000.
- [24] G. T. Bolton, K. M. Primrose. An Overview of electrical tomographic measurements in pharmaceutical and related application areas. *AAPS PharmSciTech* 6(2):E137–E143.
- [25] L. Borcea A nonlinear multigrid for imaging electrical conductivity and permittivity at low frequency. *Inverse Problems*, 17(2):329–359, 2001.
- [26] L. Borcea, J. G. Berryman, G. C. Papanicolaou. High contrast impedance tomography *Inverse Problems*, 12(6):835–858, 1996
- [27] A. Borsic, R. Halter, Y. Wan, A. Hartov, K. D. Paulsen. Sensitivity study and optimization of a 3D electric impedance tomography prostate probe. *Physiological measurement*, 30(6): S1, 2009.
- [28] A. Borsic, R. Halter, Y. Wan, A. Hartov, K. D. Paulsen. Electrical impedance tomography reconstruction for three-dimensional imaging of prostate. *Physiological measurement*, 31(8): S1, 2010.

- [29] G. B. Boverman, T. J. Kao, D. Isaacson, G. Saulnier. An implementation of calderón's method for 3-D limited view EIT. *Medical Imaging, IEEE Transactions on*, 28(7):1073–1082, 2009.
- [30] G. B. Boverman, T. J. Kao, R. Kulkarni, B. S. Kim, D. Isaacson, G. Saulnier, J. C. Newell. Robust linearized image reconstruction for multifrequency EIT of the breast. *Medical Imaging, IEEE Transactions on*, 27(10):1439–1448, 2008.
- [31] B. H. Brown. Electrical impedance tomography(EIT): a review. *Journal of Medical Engineering & Technology*, 27(3):97–108, 2003.
- [32] B. H. Brown, D. C. Barber, A. H. Morice, A. D. Leathard. Cardiac and respiratory related electrical impedance changes in the human thorax *Biomedical Engineering, IEEE Transactions on*, 41(8):729–734, 1994.
- [33] R. Brown, G. Uhlmann Uniqueness in the inverse conductivity problem for non-smooth conductivities in two dimensions. *Communications in Partial Differential Equations*, 22(5–6):1009–1027, 1997.
- [34] A. L. Bukhgeim. Recovering a potential from Cauchy data in the two-dimensional case. *Journal of Inverse and Ill-posed Problems*, 16(1):19–33, 2008.
- [35] A. P. Calderón. On an inverse boundary value problem. In *Seminar on Numerical Analysis and its Applications to Continuum Physics*, pages 65–73. Soc. Brasileira de Matemática, 1980
- [36] D. Calvetti, D. McGiveney, E. Somersalo. Left and right preconditioning for electrical impedance tomography with structural information. *Inverse Problems*, 28, 2012.
- [37] D. Calvetti, E. Somersalo Introduction to Scientific Computing- Ten lectures on Subjective Computing *New York:Springer*

- [38] M. Cheney, D. Isaacson. Distinguishability in impedance imaging. *Biomedical Engineering, IEEE Transactions on*, 39(8):852–860, 1992.
- [39] M. Cheney, D. Isaacson, E. L. Isaacson. Exact solutions to linearized inverse boundary value problem. *Inverse Problems*, 6(6):923–934, 1990.
- [40] M. Cheney, D. Isaacson, J. C. Newell, S. Simske, J. Goble. Noser: An algorithm for solving the inverse conductivity problem. *International Journal of Imaging Systems and technology*, 2(2):66–75, 1990.
- [41] M. Cheney, D. Isaacson, J. C. Newell. Electrical impedance tomography. *SIAM Review* 41(1):85–101, 1999.
- [42] V. Cherepenin, A. Karpov, A. Korjenevsky, V. Kornienko, A. Mazaletskaya, D. Mazourov, D. Meister. A 3D electrical impedance tomography (EIT) system for breast cancer detection. *Physiological measurement* 22(1):9, 2001.
- [43] M. H. Choi, T. J. Kao, D. Isaacson, G. Saulnier, J. C. Newell. A reconstruction algorithm for breast cancer imaging with electrical impedance tomography in mammography geometry. *IEEE Transactions on Biomedical Engineering*, 54(4):700-710, 2007.
- [44] W. Daily, A. Ramirez. Electrical resistance tomography during in-situ trichloroethylene remediation at the Savannah River Site. *Journal Of Applied Geophysics* 33:239–249, 1995.
- [45] W. Daily, A. L. Ramirez. Electrical imaging of engineered hydraulic barriers. *Geophysics*, 65(1):83–94, 2000.
- [46] W. Daily, A. Ramirez, D. La Brecque, J. Nitao. Electrical resistivity tomography of vadose water movement. *Water Resources Research* 28:1429–1442, 1992.
- [47] W. Daily, A. Ramirez, R. Johnson. Electrical impedance tomography of a perchloroethylene release. *Journal of Environmental and Engineering Geophysics* 2:189–201, 1998.

- [48] M. DeAngelo, J. L. Mueller. 2D D-bar reconstructions of human chest and tank data using an improved approximation to the scattering transform. *Physiological measurements*, 31(2):221–232, 2010.
- [49] R. Deiana, G. Cassiani, A. Villa, A. Bagliani, V. Bruno. Calibration of a vadose zone model using water injection monitored by GPR and electrical resistance tomography. *Vadose Zone Journal*, 7(1):215–226, 2008.
- [50] F. J. Dickin, R. A. Williams, M. S. Beck. Determination of composition and motion of multicomponent mixtures in process vessels using electrical impedance tomography-i. principles and process engineering applications. *Chemical Engineering Science* 48(10):1883–1897, 1993.
- [51] D. C. Dobson. Convergence of a reconstruction method for the inverse conductivity problem. *SIAM Journal on Applied Mathematics*, 52(2):442–458, 1992.
- [52] D. C. Dobson, F. Santosa. An image-enhancement technique for electrical impedance tomography. *Inverse Problems*, 10(2):317–334, 1994.
- [53] O. Dorn, H. Bertete-Aguirre, J. G. Berryman, G. C. Papanicolaou. A nonlinear inversion method for 3D electromagnetic imaging using adjoint fields. *Inverse Problems*, 15(6): 1523–1558, 1999.
- [54] T. Dowrick, G. S. Dos. Santos, A. Vongerichten, D. Holder. Parallel, multi frequency EIT measurement, suitable for recording impedance changes during epilepsy. *Journal of Electrical Bioimpedance*, 6(1):37–43, 2015.
- [55] A. El-Zaart, T. El-Arwadi. A new edge detection method for CT-scan lung images. *Journal of Biomedical Engineering and Medical Imaging*, 2(5), 2015.
- [56] L. D. Faddeev. Increasing solutions of the Schrödinger equation. *Soviet Doklady*, 10:1033–1035, 1966.

- [57] R. Fazel, H. M. Krumholz, Y. Wang, J. S. Ross, H. H. Chen, J. Ting, N. D. Shah, K. Nasir, A. J. Einstien, B. K. Nallamothu. Exposure to low-dose ionizing radiation from medical imaging procedures. *New England Journal of Medicine*, 361(9):849–857, 2009.
- [58] D. Ferrario, B. Grychtol, A. Adler, J. Sola, S. H. Bohm, M. Bodenstien. Toward morphological thoracic EIT: Major signal sources correspond to respective organ locations in CT. *Biomedical Engineering, IEEE Transactions on*, 59(11):3000–3008, 2012.
- [59] D. Flores-Tapia, S. Pistorius. Electrical impedance tomography reconstruction using a monotonicity approach based on a priori knowledge. In *Engineering in Medicine and Biology Society (EMBC), 2010 Annual International Conference of the IEEE*, 4996–4999, Aug 2010.
- [60] E. Francini. Recovering a complex coefficient in a planar domain from the Dirichlet-to-Neumann map *Inverse Problems*, 16(1):107–119, 2000.
- [61] D. Freimark, M. Arad, R. Sokolover, S. Zlochiver, S. Abboud. Monitoring lung fluid content in CHF patients under intravenous diuretics treatment using bio-impence measurements. *Physiological measurements*, 28(7) S269–S277, 2007.
- [62] I. Frerichs. Electrical Impedance Tomography (EIT) in applications related to lung and ventilation: a review of experimental and clinical activities. *Physiological Measurement*, 21(2):R1–R21, 2000.
- [63] I. Frerichs, J. Hinz, P. Herrmann, G. Weisser, G. Hahn, T. Dudykevych, M. Quintel, G. Hellige. Detection of local lung air content by electrical impedance tomography compared with electron beam CT. *Journal of applied physiology*, 93(2):660–666, 2002.
- [64] I. Frerichs, J. Hinz, P. Herrmann, G. Weisser, G. Hahn, M. Quintel, G. Hellige. Regional lung perfusion as determined by electrical impedance tomography in comparison with electron beam CT imaging. *Medical Imaging, IEEE Transactions on*, 21(6):646–652, 2002.

- [65] I. Frerichs, S. Pulletz, G. Elke, F. Reifferscheid, D. Schädler, J. Scholz, N. Weiler. Assesment of changes in distribution of lung perfusion by electrical impedance tomography. *Respiration*, 77(3):282–291, 2009.
- [66] I. Frerichs, G. Schmitz, S. Pulletz, D. Schädler, G. Zick, J. Scholz, N. Weiler. Reproducibility of regional lung ventilation distribution determined by electrical impedance tomography during mechanical ventilation. *Physiological Measurement*, 28(7):S261 – S 267, 2007.
- [67] R. W. Freund. A transpose-free quasi-minimal residual algorithm for non-Hermitian linear systems. *SIAM journal on scientific computing*, 14(2):470–482, 1993.
- [68] L. F. Fuks, M. Cheney, D. Isaacson, D. G. Gisser, J. C. Newell. Detection and imaging of electric conductivity and permittivity at low frequency. *Biomedical Engineering, IEEE Transactions on*, 38(11):1106–1110, 1991.
- [69] P. Gaggero, A. Adler, A. Waldmann, Y. Mamatjan, J. Justiz, V. Koch. Automated robust test framework for electrical impedance tomography. *Physiol. Meas.* 36:1227 -1244.
- [70] C. S. Gardner, J. M. Greene, M. D. Kruskal, R. M. Miura Method for solving Korteweg-de Vries equation *Physical Review Letters*, 19:1095–1097, 1967.
- [71] O. Gilad, D. S. Holder. Impedance changes recorded with scalp electrodes during visual evoked responses: implications for electrical impedance tomography of fast neural activity. *Neuroimage*, 47(2): 514–522, 2009.
- [72] A. Greenleaf, Y. Kurylev, M. Lassas, G. Uhlmann. Invisibility and Inverse problems. *Bull. Amer. Math. Soc.* 46:55-97,2009.
- [73] A. Greenleaf, M. Lassas, G. Uhlmann. Anisotropic conductivities that cannot be detected by EIT. *Physiological Measurement*, 24:413-419,2003.

- [74] M. Hallaji, A. Seppnen, M. Pour-Ghaz. Electrical impedance tomography-based sensing skin for quantitative imaging of damage in concrete. *Smart Materials and Structures*, 23(8):085001, 2014.
- [75] R. J. Halter, A. Hartov, K. D. Paulsen. A broadband high-frequency electrical impedance tomography system for breast imaging. *Biomedical Engineering, IEEE Transactions on*, 55(2):650–659, 2008.
- [76] S. J. Hamilton, M. Lassas, S. Siltanen. A Direct reconstruction method for anisotropic electrical impedance tomography. *Inverse Problems* 30:21–54, 2014.
- [77] L. M. Heikkinen, J. Kourunen, T. Savolainen, P. J. Vauhkonen, J. P. Kaipio. Real time three-dimensional electrical impedance tomography applied in multiphase flow imaging. *Measurement Science and Technology* 17(8):2083, 2006.
- [78] C. N. L. Herrera, M. F. M. Vallejo, J. L. Mueller, R. G. Lima. Direct 2-D reconstructions of conductivity and permittivity from EIT data on human chest. *IEEE Transactions on Medical Imaging*, 34(1):267–274, 2015.
- [79] J. Hola, K. Schabowicz. State-of-the-art non-destructive methods for diagnostic testing of building structures anticipated development trends. *Archives of Civil and Mechanical Engineering*, 10(3):5–18, 2010.
- [80] D. Holder, editor. *Electrical Impedance Tomography: Methods, History and Applications*. IOP Publishing Ltd., Bristol, UK, 2005.
- [81] T. C. Hou, J. P. Lynch. Electrical impedance tomographic methods for sensing strain fields and crack damage in cementitious structures. *Journal of Intelligent Material Systems and Structures*, 20(11):1363–1379, 2009.
- [82] D. Isaacson, J. L. Mueller, J. C. Newell, S. Siltanen. Imaging cardiac activity by the D-bar method for electrical Impedance tomography. *Physiological Measurement* 27(5):S43–S50, 2006.

- [83] D. Isaacson, J. L. Mueller, J. C. Newell, S. Siltanen Reconstructions of Chest Phantoms by the D-bar method for Electrical Impedance Tomography *IEEE Transactions on medical imaging* 23(7): 821– 828, 2004.
- [84] H. Jin, S. Yang, M. Wang, R. A. Williams. Measurement of gas holdup profiles in a gas liquid cocurrent bubble column using electrical resistance tomography. *Flow Measurement and Instrumentation*, 18(56):191–196, 2007.
- [85] J. Jordana, M. Gasulla, R. Pallás-Areny. Electrical Resistance Tomography to detect leaks from buried pipes *Measurement Science and Technology* 12:1061–1068, 2001.
- [86] J. Kaipio, E. Somersalo Statistical and Computational Inverse Problems *Springer*, 2004.
- [87] A. Kemna, A. Binley, A. Ramirez, W. Daily. Complex resistivity tomography for environmental applications. *Chemical Engineering Journal* 77:11–18, 2000.
- [88] C. E. Kenig, M. Salo, and G. Uhlmann. Inverse problems for the anisotropic Maxwell equations. *Duke Math J.* 157:369–419, 2011.
- [89] S. Kim, A. N. Nkaya T. Dyakowski. Measurement of mixing of two miscible liquids in a stirred vessel with electrical resistance tomography. *International Communications in Heat and Mass Transfer* 33(9):1088–1095, 2006.
- [90] R. V. Kohn, M. Vogelius. Determining conductivity by boundary measurements. *Communications on Pure and Applied Mathematics* 37(3): 289–298, 1984.
- [91] R. V. Kohn, M. Vogelius. Identification of an unknown conductivity by means of measurements at the boundary. *Laboratory for Numerical Analysis, Technical Note* BN-1005, 1983.
- [92] J. Kourunen, R. Kyhk, J. Matula, J. Kyhk, M. Vauhkonen, L. M. Heikkinen. Imaging of mixing of two miscible liquids using electrical impedance tomography and linear impedance sensor. *Flow Measurement and Instrumentation* 19(6):391–396, 2008.

- [93] H. Kwon, J. I. Choi, J. K. Seo. An Electrical impedance monitoring of water-lubricated oil transportation. *Flow Measurement and Instrumentation*, 46, Part B:327–333, 2015
- [94] A. D. Leathard, B. H. Brown, J. Campbell, F. Zhang, A. H. Morice, D. Tayler. A comparison of ventilatory and cardiac related changes in EIT images of normal human lungs and of lungs with pulmonary emboli. *Physiological Measurement* 15(2A):A137–A.
- [95] J. M. Lee, G. Uhlmann. Determining Anisotropic Real- Analytic Conductivities by Boundary Measurements. *Communications on pure and applied mathematics*, 42(8): 1097–1112, 1989.
- [96] W. R. B. Lionheart. Conformal uniqueness results in anisotropic electrical impedance imaging *Inverse Problems*, 13:125–134, 1997.
- [97] J. L. Mueller and S. Siltanen. Linear and Nonlinear Inverse Problems with Practical Applications. *SIAM*, 2012.
- [98] P. A. Muller, D. Isaacson, J. C. Newell, G. J. Saulnier. Calderón’s method on an elliptical domain. *Physiological Measurement*, 34(6):609, 2013.
- [99] E. K. Murphy, J. L. Mueller. Effect of domain-shape modeling and measurement errors on the 2-D D-bar method for electrical impedance tomography. *IEEE Trans. Med. Imaging* 28-10: 1567–1584.
- [100] A. Nachman, J. Sylvester, G. Uhlmann. An n -dimensional Borg-Levinson theorem. *Communications in Mathematical Physics*, 115(4):595–605, 1988.
- [101] A. Nachman. Reconstructions from boundary measurements. *Annals of Mathematics*, 128(3):531–576, 1988.
- [102] A. Nachman. Global uniqueness for a two-dimensional inverse boundary value problem. *Annals of Mathematics*, 143(1):71–96, 1966.

- [103] G. Nakamura, G. Uhlmann, J-N. Wang. Oscillating-decaying solutions, Runge approximation property for the anisotropic elasticity system and their applications to inverse problems. *Journal de Mathématiques Pures et Appliquées* 84-1:21–54, 2005.
- [104] J. C. Newell, P. M. Edic, X. Ren, J. L. Larson-Wiseman, M. D. Danyleiko Assessment of pulmonary edema in dogs by electrical impedance imaging. *IEEE Transactions on Biomedical Engineering*, 43(2):133–138, 1996.
- [105] D. T. Nguyen, C. Jin, A. Thiagalingam, A. L. McEwan. A review on electrical impedance tomography for pulmonary perfusion imaging. *Physiological Measurement* 33(5):695, 2012.
- [106] T. J. Noble, A. H. Morice, K. S. Channer, P. Milnes, N. D. Harris, B. H. Brown Monitoring patients with left ventricular failure y electrical impedance tomography. *European Journal of Heart Failure*, 1(4):379–384, 1999.
- [107] A. Ramirez, W. Daily, D. La Brecque, E. Owen, D. Chestnut. Monitoring an underground steam injection process using electrical resistance tomography. *Water Resources Research* 29:73–88, 1993.
- [108] A. Ramirez, W. Daily, D. J. LaBreque, D. Roelant Detection of leaks in underground storage tanks using electrical resistance method. *Journal of Environmental and Engineering Geophysics*, 1:189–203, 1996.
- [109] V. Rimpiläinen, L. M. Heikkinen, M. Kuosmanen, A. Lehikoinen, A. Voutilainen, J. Vauhkonen, M. Ketolainen An electrical impedance tomography-based approach to monitor in vitro sodium chloride dissolution from pharmaceutical tablets. *Review of Scientific Instruments* 80(10), 2009.
- [110] V. Rimpiläinen, M. Kuosmanen, J. Ketolainen, K. Jrvinen, M. Vauhkonen, L. M. Heikkinen. Electrical impedance tomography for three dimensional drug release monitoring. *European Journal of Pharmaceutical Sciences* 41(2):407–413,2013.

- [111] A. V. Shahidi, R. Guardo, P. Savard. On the monitoring of pulmonary edema by impedance tomography. In *Engineering in Medicine and Biology Society, 1994. Engineering Advances: New Opportunities for Biomedical Engineers. Proceedings of the 16th Annual International Conference of the IEEE 1994*.
- [112] J. Sylvester, G. Uhlmann. A uniqueness theorem for an inverse boundary value problem in electrical prospection *Communications on Pure and Applied Mathematics*, 39(1):91–112, 1986.
- [113] J. Sylvester, G. Uhlmann. A global uniqueness theorem for an inverse boundary value problem. *Annals of Mathematics*, 41(2):197–219, 1988.
- [114] J. Sylvester, G. Uhlmann. Inverse boundary value problems at the boundary continuous dependence. A uniqueness theorem for an inverse boundary value problem in electrical prospection. *Communications on Pure and Applied Mathematics*, 41(2):197–219, 1988.
- [115] H. Takuwa, G. Uhlmann, J. Wang. Complex Geometrical Optics Solutions for Anisotropic Equations and Applications. *Journal of Inverse and Ill-Posed Problems* 16(8), 2008.
- [116] C. J. C. Trepte, C. R. Phillips, J. Solá, A. Adler, S. A. Haas, M. Rapin, S. H. Böhm, D. A. Reuter Electrical impedance tomography (EIT) for quantification of pulmonary edema in acute lung injury. *Critical Care*, 20(1):1–9, 2015.
- [117] A. Vonk, Noordegraaf, T. J. C. Faes, A. Janse, J. T. Marcus, J. G. F. Bronzwaer, P. E. Postmus, P. M. J. M. de. Vries Noninvasive assessment of right ventricular diastolic function by electrical impedance tomography. *CHEST* 111(5):1222–1228, 1997.
- [118] R. M. West, D. M. Scott, G. Sunshine, J. Kostuch, L. Heikkinen, M. Vauhkonen, B. S. Hoyle, H. I. Schlaberg, R. Hou, R. A. Williams In situ imaging of paste extrusion using electrical impedance tomography. *Measurement Science and Technology* , 13(12):1890, 2002.

- [119] J. Zhang, R. Patterson. EIT images of ventilation: what contributes to the resistivity changes? *Physiological Measurements*, 26:S81–S92, 2005.
- [120] J. Zhang, R. Patterson. EIT images of ventilation: what contributes to the resistivity changes? *Physiological Measurements*, 26:S81–S92, 2005.